Trace metal and sulfur cycling in a hydrothermally active arc volcano: Deep-sea drilling of the Brothers volcano, Kermadec arc, New Zealand.

Andrew J. Martin[1,2*], John W. Jamieson[1], Cornel E.J. de Ronde[3], Susan E. Humphris[4], Iain McDonald[5], Graham D. Layne[1], Glenn Piercey[6] and Christopher J. MacLeod[5]

[1] Department of Earth Sciences, Memorial University of Newfoundland, Canada

[2] Department of Geoscience, University of Nevada, Las Vegas, USA

[3] GNS Science, 1 Fairway Drive, Lower Hutt 5040, New Zealand

[4] Department of Geology & Geophysics, Woods Hole Oceanographic Institution, Woods Hole, Massachusetts 02543, USA

[5]School of Earth and Environmental Sciences, Cardiff University, UK

[6] MAF-IIC SIMS Facility, Memorial University of Newfoundland, Canada

*corresponding author: andrew.martin@unlv.edu

Key words: IODP, trace metal geochemistry, sulfur isotopes, pyrite, Brothers volcano

Statements and Declarations

All authors certify that they have no affiliations with or involvement in any organization or entity with any financial interest or non-financial interest in the subject matter or materials discussed in this manuscript.

Abstract

Brothers volcano, located on the Kermadec arc north of New Zealand, hosts two geochemically distinct hydrothermal systems. The NW Caldera and Upper Cone hydrothermal fields exhibit distinct fluid compositions that are significantly influenced by seawater and magmatic volatiles, respectively. In this study, we present trace metal chemistry and sulfur isotope compositions of pyrite within hydrothermally-

altered volcanic rocks recovered from drill cores at depths of up to 429 m below the seafloor collected during the International Ocean Discovery Program's Expedition 376. Magmatic volatile-influenced alteration resulting in pyrophyllite ± natroalunite assemblages occurs at the Upper Cone and at the NW Caldera below 189 m. At the NW Caldera, a later seawater-derived hydrothermal fluid overprints magmatic volatile alteration forming chlorite-rich alteration. Pyrite at the Upper Cone is fine-grained, euhedral and enriched in Cu, As, Sb, Pb and Pt and has an average $\delta^{34}S$ composition of -5.5 ± 2.9‰ (1σ, *n= 32*). In contrast, pyrite associated with pyrophyllite-rich alteration at the older NW Caldera site is coarse-grained, subhedral and has higher Co, Se, Te and Bi contents but a comparable average $\delta^{34}S$ value of -4.8 ± 5.5‰ (1σ, *n= 26*). The difference in trace metal content between pyrite from pyrophyllite ± natroalunite assemblages at the NW Caldera and Upper Cone site indicates a change in the trace metal enrichment signature of pyrite with the age of the hydrothermal system. Pyrite from chlorite-rich alteration (NW Caldera) is depleted in Cu, Te and Bi relative to all magmatic volatile-influenced pyrite but has a similar average $\delta^{34}S$ composition of -4.6 ± 3.5‰ (1σ, *n= 20*). The similarity in trace metal enrichment signature and average $\delta^{34}S$ composition of pyrite, regardless of associated alteration mineral assemblage shows that the initial magmatic volatile trace metal signature and sulfur isotope composition of pyrite is preserved during fluid overprinting. The lower content of Cu, Te and Bi in pyrite from chlorite-rich alteration confirms the importance of seawater-derived hydrothermal fluids in metal mobilization and consequent formation of hydrothermal precipitates at the seafloor.

Introduction

The distribution of trace metals in sulfide minerals associated with seafloor hydrothermal systems is poorly constrained, with many studies focusing solely on samples collected from black smoker chimneys and massive sulfide deposits at the seafloor (Butler and Nesbitt 1999; Berkenbosch et al. 2012; Wohlgemuth-Ueberwasser et al. 2015). Only a few studies have collected samples from below the seafloor, including the active TAG mound (Humphris et al. 1995), Iheya North (Takai et al. 2011), PACMANUS (Binns et al. 2002) and Middle Valley (Fouqet et al. 1998).

47 Variations in the trace metal signature and content of sulfide minerals that precipitate during the mixing of
48 magmatic vapour and fluid with seawater can constrain the physical (e.g., temperature) and chemical (e.g.,
49 pH) composition of the hydrothermal fluid from which they formed (e.g., Metz and Trefry 2000;
50 Wohlgemuth-Ueberwasser et al. 2015; Fuchs et al. 2019). Pyrite is especially useful in constraining changes
51 in fluid chemistry and metal sources, as it is ubiquitous in seafloor hydrothermal mineral deposits
52 (Hannington et al. 2005). In addition, sulfur isotope analysis can be used to assess links between magmatic
53 volatile influx and metal enrichment in seafloor hydrothermal systems (Herzig et al. 1998; de Ronde et al.
54 2011). When combined, trace metal chemistry and the sulfur isotopic composition of pyrite can determine
55 subsurface fluid mixing regimes, variations in magmatic volatile degassing and can be used to assess the
56 movement and sequestration of metals below the seafloor.

57 Direct influx of magmatic volatiles during the degassing of shallow magma reservoirs has been suggested
58 as an important source of some metals in seafloor hydrothermal deposits (Yang and Scott 1996; Butterfield
59 et al. 2011; de Ronde et al. 2011; 2019a; Keith et al. 2016; Berkenbosch et al. 2019; Patten et al. 2020).
60 This is especially true in arc and back-arc hosted hydrothermal systems where magmas commonly reach
61 volatile saturation (Wallace 2005; Edmonds and Wallace 2017). The addition of magmatic volatiles such
62 as SO_2, H_2O, CO_2, HCl and HF are important for two reasons: i) they provide a source of acidity that can
63 directly influence the solubility and transport of metals, and ii) magmatic degassing may provide a direct
64 source of certain metals to the overlying hydrothermal systems (Yang and Scott 1996). Some authors have
65 suggested that the enrichment of Te, Se, Au, Bi and Cu provides evidence for the addition of a magmatic
66 volatile phase into seafloor hydrothermal systems (Berkenbosch et al. 2012; Keith et al. 2016; Martin et al.
67 2020), whereas others suggest enrichment in Pb, As, Sb, Hg, Mo, Ag and S (Petersen et al. 2002;
68 Wohlgemuth-Ueberwasser et al. 2015; Berkenbosch et al. 2019; Patten et al. 2020). Hence, the trace metal
69 enrichment signature associated with the addition of magmatic volatiles warrants further examination.

70 In addition to trace metal enrichment profiles, sulfur isotope ratios ($\delta^{34}S$) of sulfide minerals can be used to
71 investigate contributions from different, isotopically distinct sources of sulfur in the hydrothermal fluids.

Sulfide minerals in arc and immature back-arc seafloor hydrothermal deposits commonly have $\delta^{34}S$ values that are <0‰, such as Hine Hina (Lau back-arc basin; Herzig et al. 1998), Conical Seamount (near Lihir Island: Petersen et al. 2002; Gemmell et al. 2004) or SuSu Knolls (Yeats et al. 2014) indicating that the disproportionation of SO_2 occurs widely in these environments forming ^{34}S depleted sulfides (Ohmoto and Lasaga 1982; Kusakabe et al. 2000; Peters et al. 2021).

Here we present the trace metal geochemistry and sulfur isotope composition ($\delta^{34}S$) of pyrite from below the seafloor at the Brothers volcano collected during the International Ocean Discovery Program's (IODP) Expedition 376: "Brothers Arc Flux". At Brothers, based on the alteration mineralogy of volcanic host rocks and the chemistry of vent fluid, both magmatic volatile and seawater-influenced hydrothermal systems have been identified (de Ronde et al. 2005, 2011, 2109a). The Upper Cone site represents a relatively young magmatic-hydrothermal system, whereas the NW Caldera site is older and contains evidence of both seawater-derived and magmatic volatile-influenced alteration (de Ronde et al. 2019a). These two distinct styles of hydrothermal venting (de Ronde et al. 2011) allow us to establish links between magmatic volatile influx and the enrichment of trace metals in pyrite, and how this signature is affected by later seawater-derived hydrothermal fluid overprinting. This makes the Brothers volcano an ideal location to evaluate how the trace metal and sulfur isotopic composition of pyrite varies between hydrothermal fields, with depth below the seafloor, and to link metal enrichment signatures to magmatic volatile influx, system age, and subsurface fluid mixing.

Brothers volcano

Brothers volcano is located in the southern part of the Kermadec-Tonga intraoceanic arc, north of New Zealand (de Ronde et al. 2012; Fig. 1). The volcano consists of an elongate NW-SE volcanic edifice with a prominent central caldera with a near continuous rim measuring 3 x 3.4 km (de Ronde et al. 2005; Embley et al. 2012; Fig. 2). The volcanic rocks within the volcano are largely dacitic with minor rhyolitic lavas and

rare basaltic dikes (Wright and Gamble 1999; Haase et al. 2006; Timm et al. 2012; Wysoczanski et al. 2012).

In this study we present data collected during IODP Expedition 376 from two drill holes within Brothers volcano (Fig. 2A). Hole U1530A is located in the NW Caldera hydrothermal field on the faulted inner caldera wall at a water depth of 1594.9 meters below sea level (mbsl) where drilling penetrated to a depth of 453 mbsf with an overall core recovery rate of 16.9% (de Ronde et al. 2019b). Hole U1528D is located in a crater atop the volcanic Upper Cone at a water depth of 1229.1 mbsl where drilling penetrated to a maximum depth of 359 mbsf with an overall core recovery rate of 26.1% (de Ronde et al. 2019c).

Hydrothermal venting

Brothers volcano hosts five active and one inactive site of hydrothermal venting (de Ronde et al. 2005; Baker et al. 2012). In this study, we focus on the NW Caldera and Upper Cone fields that show morphologically and geochemically distinct styles of hydrothermal venting. Fluid flow at the NW Caldera vent field occurs on the inner caldera wall and is controlled by a series of ring faults (Fig. 2B; Embley et al. 2012; Caratori Tontini et al. 2012, 2019; de Ronde et al. 2019a). Here, high-temperature (up to 320 °C), moderately acidic (pH 3.2), gas poor fluids that contain high Cl contents (up to 787 mM/kg; Kleint et al. 2019) are actively venting and forming metal-sulfide-rich chimneys. In contrast, the Upper Cone is characterized by diffuse fluid venting forming native sulfur chimneys and Fe-oxide crusts (Fig. 2A; de Ronde et al. 2011; Kleint et al. 2019; Stucker et al. 2022). At the Upper Cone, vent fluids are highly acidic (pH 1.2) but with lower temperatures (maximum 122 °C) and contain elevated ΣSO_4 ($\leq$88.9 mM) and H_2S (5.0 mM) contents (de Ronde et al. 2011; Kleint et al. 2019).

Alteration mineralogy

The difference in fluid chemistry and temperature between the Upper Cone and NW Caldera vent sites is reflected in the alteration mineralogy of the underlying volcanic rocks (de Ronde et al. 2019a, b, c,).

Previous studies have identified five different alteration mineral assemblages, two at the NW Caldera and three at the Upper Cone (Fig. 3 and 4) (de Ronde et al. 2019b; Martin et al. 2022).

At the NW Caldera site, alteration containing chlorite + quartz + anhydrite + pyrite ± illite ± smectite, classified as chlorite + quartz alteration, formed from the circulation of high-temperature (~300 °C), moderately low-pH (3-4) seawater-derived hydrothermal fluids. In contrast, pyrophyllite + illite + anhydrite + quartz + pyrite ± rutile ± diaspore ± zunyite, classified as pyrophyllite + illite alteration, indicates the presence of high-temperature (>320 °C) acidic fluids (pH <3) (de Ronde et al. 2019c; Martin et al. 2022) (ESM 1, Table T1 for sample description). Based on the distribution of alteration minerals with depth below the seafloor, a two-stage model has been proposed for the magmatic-hydrothermal evolution of Brothers volcano (de Ronde et al. 2019a). At the NW Caldera, below 189 mbsf, magmatic volatile-influenced alteration containing pyrophyllite + illite is locally overprinted by a chlorite + quartz assemblage (Fig. 3A-1) (de Ronde et al. 2019a,b). Overprinting results from changes in near-surface permeability that occurred in response to caldera collapse, which facilitated seawater ingress along caldera bounding ring faults and through the fractured caldera floor (Caratori Tontini et al. 2019; de Ronde et al. 2019a). The circulation of modified seawater and its consequent interaction with the host rocks led to the remobilization of earlier formed (by the magmatic fluids) hypersaline metal-rich brines within the NW Caldera hydrothermal system, providing a metal source for overlying seafloor sulfide mineralization (de Ronde et al. 2011, 2019a; Berkenbosch et al. 2012; Gruen et al. 2014).

At the Upper Cone, samples that contain natroalunite + anhydrite + quartz + cristobalite ± illite ± native sulfur ± pyrite ± rutile, classified as natroalunite alteration, formed at high-temperatures (>300 °C) from low-pH (<1-2) “acid-sulfate” type fluids. Samples that contain pyrophyllite + natroalunite + anhydrite + quartz + cristobalite ± native sulfur ± pyrite ± rutile, classified here as natroalunite + pyrophyllite alteration, formed at comparably high-temperatures (~300 °C) but at lower water:rock ratios (Seewald et al. 2019). In contrast, some samples contain smectite + cristobalite + pyrite + anhydrite and primary igneous plagioclase is preserved, indicating regions of increased seawater influx characterized by lower fluid temperatures

144 (~180 °C) and a higher fluid pH (~5) (Martin et al. 2022). These three mineral assemblages occur
145 intercalated at irregular depth intervals from the seafloor to the bottom of the hole at the Upper Cone (Fig.
146 4A-1).

147 Methods

148 Trace element geochemistry of pyrite

149 The trace metal content of pyrite was analyzed by laser ablation inductively coupled plasma mass
150 spectrometry (LA-ICP-MS) using a New Wave Research UP213 UV laser coupled to an iCAP RQ ICP-
151 MS (*n= 345*; ESM 1, Table T3-5). Point analyses were performed with a diameter of 40 µm in time resolved
152 analysis mode at a frequency of 10 Hz. Acquisition lasted for 45 s and a gas blank was measured for 25 s
153 prior to analysis. Analyte masses measured included: ^{59}Co, ^{60}Ni, ^{65}Cu, ^{66}Zn, ^{75}As, ^{77}Se, ^{99}Ru, ^{101}Ru, ^{103}Rh,
154 ^{105}Pd, ^{106}Pd, ^{108}Pd, ^{109}Ag, ^{111}Cd, ^{121}Sb, ^{125}Te, ^{185}Re, ^{189}Os, ^{193}Ir, ^{195}Pt, ^{197}Au, ^{206}Pb and ^{209}Bi. Data correction
155 and the subtraction of gas blanks was performed using Thermo Qtegra software. External calibration was
156 performed on a series of in-house sulfide standards (see Prichard et al. 2013). The repeat analysis of
157 standard UQAC FeS-1 during analysis yielded a relative standard deviation of <5% for all elements except
158 Ni, Cu and Cd, which were 17, 17 and 26%, respectively (ESM 1, Table T2). Sulfur-33 was used as an
159 internal standard for all LA-ICP-MS analyses. The sulfur content of pyrite was determined prior to LA-
160 ICP-MS analysis using quantitative energy dispersive spectroscopy on a scanning electron microscope,
161 yielding an average sulfur content of 54.1 ± 0.4 wt.% (1σ, *n= 359*; ESM 1, Table T6).

162 Sulfur isotope analysis

163 The sulfur isotope composition (δ^{34}S) of pyrite was determined using secondary ion mass spectrometry
164 (SIMS) microanalysis. Seventy-eight analyses were performed across 28 polished mounts that represent
165 the different alteration mineral assemblages identified at Brothers. Sample blocks were mounted in epoxy
166 in aluminum retaining rings, polished, and coated with 300Å of Au prior to analysis to mitigate charging
167 of the sample during ion bombardment. Samples were analyzed using a Cameca IMS 4f SIMS instrument

at the Microanalysis Facility at Memorial University of Newfoundland following the analytical procedure detailed in Brueckner et al. (2015). Each sample was bombarded with a primary ion beam of 250-450 pA of Cs^+ accelerated through a potential of 10 keV and focused into a 10 µm diameter rastered spot. Negatively charged secondary ions were accelerated into the mass spectrometer using a potential of +4.5 keV. Prior to analysis, each spot was pre-sputtered for 120 s with a 10 µm rastered beam to exclude sulfur contamination from the sample surface. Reproducibility of results was calculated based on the repeat analysis of standard reference materials UL9 (pyrite - $\delta^{34}S$= 16.3‰) and KH87 (pyrite - $\delta^{34}S$= 0.4‰) and is typically better than ±0.4‰ (1σ, ESM 1, Table T7). All analyses are reported in standard notation (‰) relative to Vienna-Canyon Diablo Troilite (VCDT).

Results

Sample mineralogy

We retain the use of previous classifications based on alteration mineralogy with samples from the NW Caldera wall (Hole U1530A) classified into chlorite + quartz and pyrophyllite + illite alteration assemblages (de Ronde et al. 2019a,b; Martin et al. 2022). Pyrite in the chlorite + quartz alteration (Fig. 3A and B) is relatively coarse-grained (>0.2 mm) and subhedral to euhedral (Fig. 3D, E and F). In the pyrophyllite + illite-rich (Fig. 3C) samples, pyrite is associated with anhydrite veins that cut the wall rock alteration (Fig. 3G). Sphalerite occurs as micro-scale inclusions within subhedral coarse-grained (>0.2 mm) pyrite (Fig. 3H). Some pyrite grains in pyrophyllite-rich alteration are anhedral (Fig. 3I). When etched using NaOCl, pyrite grains exhibit a range of different internal zonation patterns (Fig. 3J to L). In pyrite from samples located near the seafloor (<31 mbsf), multiple radial zonations parallel to the grain margin that delineate overgrowths are present (Fig. 3J). In deeper samples from chlorite + quartz alteration, zonations in pyrite are more diffuse and appear chaotic with crystal faces poorly defined (Fig. 3K). Pyrite from pyrophyllite + illite alteration commonly contained radial zonations that are no longer parallel to the grain margin, delineating a relict inner core zone (Fig. 3L).

192 At the Upper Cone (Hole U1528D) natroalunite + pyrophyllite ± native sulfur alteration occurs
193 preferentially along bleached selvage networks that overprint the brecciated matrix (Fig. 4A). In some
194 samples where bleached selvages are absent and alteration is more pervasive, pyrophyllite is absent (Fig.
195 4B). In other samples, both pyrophyllite and natroalunite are absent and samples contain smectite with the
196 preservation of primary plagioclase (Fig. 4C). In all samples, pyrite occurs as very finely disseminated
197 euhedral to subhedral grains (Fig. 4D-I). Pyrite occurs intergrown in the sample matrix (Fig. 4 D-F),
198 associated with natroalunite + anhydrite that replaces plagioclase (Fig. 4G), and infilling vugs (Fig 4. H
199 and I) (de Ronde et al. 2019b). Pyrite from the Upper Cone rarely displayed any internal zonation (Fig. 4J).
200 In aggregates of pyrite, some grains showed radial zonations parallel to the grain margins (Fig. 4K and L)

201 ## Pyrite chemistry

202 ### NW Caldera

203 Six representative polished mounts were analyzed from the chlorite + quartz alteration (*n= 53* spot analyses;
204 Fig. 5, Table 1) and nine mounts from samples with pyrophyllite + illite alteration assemblages at the NW
205 Caldera site (*n= 76* spot analyses; Fig. 5). The pattern of enrichment for all pyrites at both the Upper Cone
206 and NW Caldera, regardless of alteration assemblage show a relative enrichment in Cu, Se, Te and Pb
207 compared to other elements analyzed (e.g., As, Sb, Bi, Co; Fig. 5A). However, the trace metal content of
208 pyrite is variable between the different alteration mineral assemblages (Fig. 5A). Pyrite from the chlorite +
209 quartz-rich alteration is enriched in As, Sb, Au and Pb, and depleted in Co, Cu, Se, Te and Bi, relative to
210 pyrite from pyrophyllite + illite alteration (Fig. 5). Pyrite from the pyrophyllite + illite samples of Hole
211 U1530A is strongly enriched in Se and Co relative to pyrite from Hole 1528D of the Upper Cone (Fig 5A).

212 A moderate positive correlation is observed between Au and Ag (R^2=0.62), Pb (R^2=0.67), Te (R^2=0.69),
213 and Bi (R^2=0.63) and a strong correlation between Re and Pt (R^2=0.89) in pyrite from chlorite + quartz
214 samples. In pyrite from pyrophyllite + illite samples, a strong correlation exists between Zn and Cd (R^2=
215 0.92) with a moderate to strong correlation between Se and Cu (R^2=0.63) and Se and Ag (R^2=0.81) (ESM
216 1, Table T4).

In addition to the difference in trace metal content between alteration types, trends also exist with depth below the seafloor. Near seafloor chlorite-rich samples to a depth of 26 mbsf are strongly enriched in As, Sb, Pb and Ag relative to deeper samples (Fig. 6A). Cobalt, Zn, Se, Te and Bi contents of near seafloor samples were generally below detection limit (Fig. 6A). With increasing depth, the median Co content of pyrite increases, peaking at a depth of 314 mbsf with a median content of 90 ppm (*n= 7*), then decreases to similar contents observed for the shallow parts of the core. Pyrite in pyrophyllite + illite samples at a depth of between 232 and 415 mbsf contained median Cu, Sb and Pb contents below the detection limit (Fig. 6A).

Upper Cone

Pyrite was analyzed in 17 polished mounts from the Upper Cone site (*n= 216* spot analyses; Fig. 5, Table 1). Pyrite from the smectite + primary plagioclase samples is enriched in As, Te, Pb, and Bi relative to other alteration types for this site (Fig. 5D, F, H and M), and contains the highest total measured trace metal content at 429 ppm (*n= 28*). Natroalunite + pyrophyllite samples contain the highest median Cu and Se contents but have the lowest median Co, As and Bi contents (*n= 151*; Fig. 5). Pyrite from natroalunite-rich samples contain the highest median Sb content but have the lowest median Se and Te contents (*n= 37;* Fig. 5G and H).

In the smectite + primary plagioclase samples, a moderate to strong positive correlation occurs between As and Sb ($R^2 = 0.69$), Ag and Pb ($R^2 = 0.88$), Sb and Pb ($R^2 = 0.77$), and Au and Pb ($R^2 = 0.66$). In pyrite from the natroalunite + pyrophyllite samples, only Zn and Ag ($R^2 = 0.74$), and Cd ($R^2 = 0.55$) show notable correlation. In the natroalunite-rich samples, a strong positive correlation exists between Pt and Re ($R^2 = 0.95$) and Au ($R^2 = 0.87$), with a moderate correlation between Pb, Au and Ag ($R^2 = 0.64$) (ESM 1, Table T5).

In addition to variations in pyrite chemistry with alteration assemblage, the trace metal content of pyrite varies with depth below the seafloor at the Upper Cone site (Fig. 6B). Pyrite from the uppermost 153 mbsf of the core has a higher trace metal content relative to pyrite from samples deeper in the hole. For example,

241 the median Cu content of pyrite above 153 mbsf is 493 ppm, decreasing to 107 ppm below this depth (Fig.
242 6B). Similar enrichments in Se, Bi and Te are also noted above 153 mbsf.

243 Sulfur isotopes

244 NW Caldera

245 The sulfur isotope composition of pyrite from NW Caldera Hole U1530A range from -13.2 to 3.8‰, with
246 an average $\delta^{34}S$ value of -4.7 ± 4.4‰ (1σ, *n= 46*). Pyrite from chlorite + quartz-rich samples range from -
247 12.9‰ to 0.4‰ and have an average $\delta^{34}S$ value of -4.6 ± 3.5‰ (1σ, *n= 26*), whereas pyrite from the
248 pyrophyllite + illite samples range from -13.2‰ to 3.8‰ but with a similar average $\delta^{34}S$ value of -4.8 ±
249 5.5‰ (1σ, *n= 20*; Fig. 7).

250 With the exception of pyrite from a pyrophyllite + illite sample, core section (65R1), located at a depth of
251 314 mbsf, the average $\delta^{34}S$ composition of all samples was <0‰ (Fig. 8A). Only minor trends are
252 discernible between sulfur isotope composition and depth below seafloor (Fig. 8A). For example, in the
253 uppermost 50 mbsf, average $\delta^{34}S$ values appear to broadly decrease with depth from -1.5‰ at 0.7 mbsf to
254 -6.7‰ at a depth of ~40 mbsf (Fig. 8A). Below a depth of 189 mbsf, $\delta^{34}S$ values in pyrite become more
255 sporadic and no trends are discernible.

256 Upper Cone

257 The sulfur isotopic composition of pyrite from the Upper Cone ranges between -12.2 and 0.3‰, with
258 samples dominated by smectite + primary plagioclase having an average value of -6.4 ± 2.8‰ (1σ, *n= 7*),
259 compared with -5.2 ± 2.6‰ (1σ, *n= 17*) and -5.0 ± 3.8‰ (1σ, *n= 8*) for samples that contain only
260 natroalunite and natroalunite + pyrophyllite, respectively. There is no systematic relationship between
261 pyrite sulfur isotope composition and depth below the seafloor (Fig. 8B).

Discussion

Incorporation of trace metals in pyrite

Trace metal content in pyrite can occur in two ways: i) lattice bound substitution, or ii) nano- to micro-scale inclusions analyzed within the host pyrite (Huston et al. 1995; Reich et al. 2005; Deditius et al. 2011). The incorporation of metals via substitution is dependent on the ionic radii and difference in charge between the elements that are being substituted (Goldschmidt and Muir 1954). In pyrite, metals are incorporated either through the substitution of Fe^{2+} (e.g., Co^{2+}) or S^{2-} (e.g., Se^{2-}), with substitutions being either stoichiometric (e.g., Co) or non-stoichiometric (e.g., Au or As; Abraitis et al. 2004).

Pyrite is the only sulfide mineral observed at the Upper Cone site. At the NW Caldera site pyrite is the dominant sulfide mineral, with minor sphalerite (<5 modal %) occurring near the seafloor (<31 mbsf) and as micro-scale inclusions in pyrite at a depth of 314 mbsf (Fig. 3H; de Ronde et al. 2019c). The presence of a mono-mineralic sulfide system is important to note, as the co-precipitation of different sulfide minerals will affect the behaviour of the trace metals (Huston et al. 1995; Cook et al. 2009; George et al. 2016). For example, Cd is preferentially incorporated in sphalerite whereas Ag preferentially partitions into galena (George et al. 2016). Therefore, pyrite that is co-precipitated with sphalerite is expected to be depleted in Zn and Cd relative to other samples that contain only pyrite. As the majority of samples from Brothers volcano are essentially mono-mineralic, it is unlikely that variation in pyrite trace metal content is influenced by the co-precipitation of different sulfide minerals.

At Brothers, pyrite textures indicating disequilibrium precipitation such as colloform or dendritic grain morphologies (Large et al. 2009; Melekestseva et al. 2014; Wohlgemuth-Ueberwasser et al. 2015) are absent in sub-seafloor samples. There is no notable variation in pyrite texture with depth below the seafloor, nor is there any notable textural variation between NW Caldera and Upper Cone pyrites. Instead, all pyrite is disseminated and anhedral to euhedral, reflecting varying degrees of grain resorption and overgrowth that occurred during the dissolution and re-precipitation of pyrite as the mineral grain grew (Figs. 3 and 4).

Grain dissolution is most prevalent in Hole U1530A at the NW Caldera where pyrite in pyrophyllite + illite-rich samples is often anhedral and highly resorbed containing relict cores (Fig. 3I and L). Thus, differences in pyrite morphology at Brothers are not considered an important factor in controlling the distribution of trace metals.

Previous studies have characterized the solubility limits of different metals in pyrite, i.e., the maximum metal content that can be hosted as a lattice bound substitution; above this threshold inclusions can form (Huston et al. 1995). Elements such as Se, Te, Au, As and Co occur in low concentrations, less than the established solubility limit for pyrite (Huston et al. 1995) indicating that they are incorporated as a lattice bound substitution (Figs. 9 and 10). Incorporation in a lattice bound substitution is confirmed using time resolved analysis (TRA) where Bi, Co, Se, Ag, Sb and Bi have a flat and uniform TRA profile that mirrors major metals such as Fe (Fig. 9A and B). Mineral inclusions, detected as discrete spikes in the TRA profile, were present in some samples (Cook et al. 2009; Wohlgemuth-Ueberwasser et al. 2015). In a sample from Hole U1528D of the Upper Cone at 191 mbsf (Fig. 9B), the TRA profile for both Zn and Cu appears jagged with distinct peaks in Zn and Cu counts confirming the presence of mineral inclusions, most likely sphalerite and chalcopyrite (Fig. 9B). The occurrence of sphalerite inclusions is also indicated in pyrophyllite + illite samples at the NW Caldera by a strong positive correlation between Zn and Cd (R^2 = 0.92), which reflects preferential partitioning of Cd into sphalerite (Cook et al. 2009).

For Au in pyrite, all data plots below the solubility limit for Au hosted as Au^0 in nano- or mineral-scale inclusions (Fig. 10A), indicating that Au is incorporated as Au^{+1} in the pyrite crystal lattice (Reich et al. 2005; Deditius et al. 2014). This is further supported by the relatively flat ablation profile for Au indicating it is incorporated in a solid solution (Fig. 9A and B). Previous studies have shown that the incorporation of Te is influenced by As content due to distortions in the pyrite lattice that occur at elevated As contents (Fig. 10B; Reich et al. 2005; Keith et al. 2018a). A large proportion of Brothers pyrite data, especially from pyrite in the chlorite + quartz-rich samples, plot above the Te solubility line indicating that Te is hosted as both inclusions and to a lesser extent as a lattice bound substitution (Fig. 10B). A similar coupled relationship

between As and Sb is also observed, indicating that As content is important in enhancing the substitution of Sb in pyrite at Brothers (Fig. 10C) (Arbraitis et al. 2004).

Trace element and sulfur isotopic variation in Brothers volcano

Influence of fluid parameters on trace metal composition of pyrite

The physical and chemical compositions of vent fluid (e.g., pH, temperature, salinity) at the NW Caldera and Upper Cone sites are distinctly different (de Ronde et al. 2011; Kleint et al. 2019; Stucker et al. 2022 indicating different sub-surface fluid mixing regimes and variable amounts of magmatic volatile influx between these sites. The formation of high-temperature (up to 320 °C; de Ronde et al. 2019a) black smokers and associated sulfide accumulations at the seafloor indicate that hydrothermal fluid at the NW Caldera did not cool substantially during its ascent through the hydrothermal system, indicating minimal sub-surface mixing between hydrothermal fluid and seawater recharge (Caratori Tontini et al. 2019). At the Upper Cone, the temperature of venting fluid at the seafloor is notably less (maximum 122 °C) than the maximum homogenization temperature of 357 °C measured in fluid inclusions in core sampled below the seafloor (de Ronde et al. 2019c). This difference in temperature indicates that extensive subsurface mixing between magmatic-hydrothermal fluids and seawater has taken place, where seawater is entrained through the walls of the Upper Cone, prior to the venting of the fluid at the seafloor (de Ronde et al. 2011; Caratori Tontini et al. 2019; Kleint et al. 2019; Stucker et al. 2022).

Understanding variations in subsurface fluid flow is important, as the temperature and pH of the hydrothermal fluid influences the solubility, incorporation and content of trace metals in pyrite (Metz and Trefry, 2000; Wohlgemuth-Ueberwasser et al. 2015). Pyrite precipitated from low-temperature fluid (<250 °C) is observed to be enriched in Au, As, Zn, Cd, Ag and Sb as these metals are stable in lower temperature hydrothermal fluids (Hannington et al. 1995; Monecke et al. 2016). In contrast, at high-temperatures (>300 °C) pyrite is enriched in Co, Te, Se, Bi and Cu (Large 1992; Butler and Nesbitt 1999; Grant et al. 2018). The approximate formation temperature of samples from below the seafloor at Brothers has been constrained using alteration mineralogy, fluid inclusion analysis on drill core samples and the direct

measurement of borehole fluid temperature (de Ronde et al. 2011, 2019b, c). The lowest temperature mineral assemblage of smectite with preservation of primary plagioclase at the Upper Cone formed at temperatures of ~180 °C (Reyes 1990) and pyrite in these samples is enriched in As, Te, Pb, and Bi (Fig. 5A and 10C). However, the enrichment of pyrite in Te and Bi is not consistent with pyrite formation at low-temperatures, indicating an additional control on the distribution of trace metals.

At the NW Caldera, pyrophyllite + illite alteration that formed at temperatures in excess of 300 °C contains the highest median Co and Se content in pyrite, although the pyrite is depleted in As, Sb and Pb. High Co and Se contents are consistent with the formation of pyrite at high-temperatures (Fig. 5A). However, pyrite from the chlorite + quartz alteration that also formed at high-temperatures (>280 °C) is relatively depleted in Se, Te, Co and Bi compared to pyrite in pyrophyllite + illite alteration, again indicating an additional control on the distribution of metals in pyrite at Brothers.

Phase separation is inferred to be an important process at the NW Caldera and Upper Cone sites (de Ronde et al. 2019a; Kleint et al. 2019; Diehl et al. 2020). At the NW Caldera, vent fluids exhibit both low and high chlorinity (310 to 751 mM; Kleint et al. 2019) relative to seawater, indicating that phase separation of the hydrothermal fluid is occurring. At the NW Caldera, anhydrite and quartz hosted fluid inclusions contain salinities of ~10 wt.% NaCl, suggesting boiling or flashing of the fluid during depressurisation, and inclusions with a salinity of ~45 wt.% NaCl equivalent that formed during the exsolution of a brine from a silicate melt (de Ronde et al. 2019a). At the Upper Cone, fluid inclusion salinities range from less than seawater (<3.2 wt.% NaCl equivalent) to ~40 wt.% NaCl equivalent (de Ronde et al. 2091a, c). The highly variable NaCl content of fluid inclusions at the Upper Cone provides evidence of vapour condensation during cooling, flashing or boiling of ascending fluid and, in the case of highly saline brines, direct exsolution from a silicate melt (de Ronde et al. 2019a,c).

Phase separation affects the concentration and distribution of trace metals in pyrite (Román et al. 2019). The partitioning of trace metals reflects the preferential segregation of Se, Te, Hg, Bi, Tl and volatiles (H_2S, CO_2, SO_2) into the vapor phase whilst Fe, Ni, Co, Pb and Zn are concentrated in the liquid phase and As

and Sb do not show any preferential partitioning during segregation (Pokrovski et al. 2013). Hence, the ratio of Bi/Pb or Sb/Pb can be used to distinguish between boiling and non-boiling assemblages (Fig. 10D) (Román et al. 2019; Nestmeyer et al. 2021).

At the NW Caldera, samples from chlorite + quartz alteration located at ~31 mbsf and a single analysis from pyrophyllite + illite alteration plot within the boiling induced precipitation field of Román et al. (2019) (Bi/Pb (<0.03) and Sb/Pb (<0.5)), providing evidence that phase separation is occurring in the shallow part of the NW Caldera hydrothermal system (Fig. 10D). At the Upper Cone, pyrite plots within the boiling field, providing evidence that phase separation is occurring throughout the Upper Cone (Fig. 10D). However, interpreting these trace metal enrichment signatures is complicated by the addition of metals from magmatic volatile degassing (Bi; Berkenbosch et al. 2019) or the remobilization of metals after initial pyrite formation.

Magmatic volatile degassing

The degassing of volatiles (e.g., SO_2, CO_2, HCl, H_2O) from shallow, volatile-saturated magma chambers in arc and back-arc hosted hydrothermal systems, has been suggested as a source of some metals in overlying seafloor hydrothermal deposits (Hedenquist and Lowenstern 1994; Yang and Scott 2002, 1996; de Ronde et al. 2011; Edmonds and Wallace 2017). The specific metal enrichment signature associated with this process remains actively debated, with previous studies indicating an enrichment in Cu, Se, Te, Au, Bi, As, Hg, Sb and Tl as evidence for magmatic volatile influx (Large 1992; de Ronde et al. 2011; Berkenbosch et al. 2012, 2019; Wohlgemuth-Ueberwasser et al. 2015; Keith et al. 2016; Martin et al. 2020; Patten et al. 2020).

To investigate the effect of magmatic volatile influx on trace metal signatures in pyrite, we compare pyrite from natroalunite and pyrophyllite-bearing alteration at both the Upper Cone and NW Caldera sites, with pyrite from chlorite + quartz alteration zones that represent magmatic and seawater-overprinted end member alteration types, respectively. We find that Co, Cu, Se, Te and Bi contents are highest in pyrite from pyrophyllite-rich alteration compared with pyrite that has been overprinted by seawater (Fig. 5 and

10). A similar signature has previously been identified in pyrite from arc related seafloor hydrothermal deposits (e.g., Hine Hina, or Volcano 19; Fig. 10), showing that increased Co, Cu, Se, Te and Bi contents in pyrite are a consequence of magmatic volatile degassing. This trace metal signature is in good agreement with previous studies that attribute the enrichment of Au, Te, Bi, Cu, Mo, Ag and Se in black smoker chimneys at the Brothers NW Caldera site to magmatic volatile degassing (Berkenbosch et al. 2019).

Elevated Se contents are widely used as an indicator of magmatic volatile influx in seafloor hydrothermal deposits and ancient volcanogenic massive sulfide deposits (Layton-Matthews et al. 2013). Experimental modelling indicates that Se incorporation in pyrite is enhanced at low-temperatures (<150 °C) under oxidizing fluid conditions (Huston et al. 1995). Therefore, Se in pyrite from natroalunite bearing alteration at the Upper Cone should contain elevated Se contents relative to all other samples, as alteration fluids are oxidizing and magmatic volatiles are actively degassing; however, this is not the case. We attribute the relative depletion of Se in pyrite from samples containing natroalunite at the Upper Cone to mineral scale partitioning of Se between coexisting native sulfur and pyrite. Natroalunite bearing alteration contains native sulfur that commonly occurs infilling secondary porosity (Fig. 4A) indicating that it formed through SO_2 disproportionation during mixing with seawater (de Ronde et al. 2011). Native sulfur analyzed from the Kueishantao volcano (offshore Taiwan), Daikoku and Nikko volcanoes (Mariana arc) and Macauley cone (Kermadec arc) contained a median Se content of 1305 ppm (*n= 56*; Zeng et al. 2007; de Ronde et al. 2015). This demonstrates the ability of native sulfur to incorporate high concentrations of Se; however, this has not been confirmed at Brothers as no native sulfur was analyzed in this study.

Sulfur isotope ratios in pyrite provide further evidence supporting the influx of magmatic volatiles at Brothers. In MOR-hosted hydrothermal deposits, sulfur is leached from oceanic lithosphere, contained primary magmatic sulfide minerals (~0.1 ± 0.5‰; Sakai et al. 1984) and the thermochemical sulfate reduction (TSR) of seawater (~21 ± 0.2‰; Rees et al. 1978). In unsedimented arc and back-arc environments, isotopically light sulfur is produced during disproportionation of SO_2 from the degassing of underlying magma chambers, producing sulfide minerals with a $\delta^{34}S$ composition <0‰ (Herzig et al. 1998;

de Ronde et al. 2011). Upon mixing with hydrothermal fluid and cooling below ~400 °C, SO_2 undergoes disproportionation, producing both oxidized SO_4^{2-} and reduced H_2S (Giggenbach 1996; Kusakabe et al. 2000). During disproportionation, SO_4^{2-} becomes enriched whilst H_2S becomes depleted in ^{34}S relative to the starting SO_2 isotopic composition. The amount of fractionation between sulfur species is dependent on temperature and the relative amount of reduced and oxidized sulfur species produced (Kusakabe et al. 2000; McDermott et al. 2015).

Previous sulfur isotope studies of sulfide chimneys and mineralized crusts from the seafloor at Brothers describe largely negative $\delta^{34}S$ values for pyrite, ranging from -5.6 to 2.1‰, with an average of -2.3 ± 1.9‰ (1σ, *n= 25*, Fig. 11; de Ronde et al. 2003, 2011, 2005). When compiled based on location, pyrite separates recovered from the Upper Cone have an average $\delta^{34}S$ value of -4.5 ± 0.7‰ (1σ, *n=4*; de Ronde et al. 2005) whilst native sulfur has a lower average $\delta^{34}S$ value of -5.3 ± 1.9‰ (1σ; *n=14*) and vent fluid HS^- averages -3.6 ± 2.1‰ (1σ, *n= 4*) (de Ronde et al. 2005, 2011). Pyrite from the NW Caldera averages -1.2 ± 2.2‰ (1σ, *n= 24*), sphalerite -2.1 ± 1.8‰ (1σ, *n= 27*), chalcopyrite -2.6 ± 1.5‰ (1σ, *n= 9*) and vent fluid HS^- -1.1 ± 0.7‰ (1σ, *n= 6*; de Ronde et al. 2003, 2005, 2011) (Fig. 11).

The predominantly negative sulfur isotope values in pyrite, native sulfur and vent fluid HS^- at the Upper Cone site has previously been attributed to the disproportionation of SO_2 degassed from an underlying magma chamber. In contrast, the occurrence of both low and high $\delta^{34}S$ values in sulfide minerals and vent fluid HS^- from the NW Caldera indicate that sulfur is sourced from a combination of SO_2 disproportionation, the leaching of host rocks and TSR of seawater (de Ronde et al. 2003, 2005, 2011).

The sulfur isotopic composition of pyrite in this study is broadly consistent with previous interpretations at Brothers that indicate widespread disproportion of SO_2 (Fig. 6). However, our data for pyrite shows a greater range than that of the previous studies, with values ranging from -13.2 to 3.8‰ at the NW Caldera, and -12.2 to 0.3‰ at the Upper Cone (Fig. 6). High values up to 3.8‰ could indicate TSR of seawater or the reduction of SO_4^{2-} produced during the disproportionation of SO_2. However, multiple sulfur isotope analysis of pyrite ($\Delta^{33}S$) is needed to investigate this further (McDermott et al. 2015).

Influence of seawater overprinting at the NW Caldera site

In Hole U1530A of the NW Caldera site, alteration associated with magmatic volatiles is overprinted by a chlorite + quartz-rich alteration assemblage in intervals below 189 mbsf, indicative of the interaction of seawater-derived hydrothermal fluids with the volcanic host rocks at temperatures >300 °C (Humphris and Thompson 1978). Mass balance calculations in oceanic crust have shown that metals are leached from host rocks during fluid-rock interactions under similar conditions (Richardson et al. 1987; Banerjee et al. 2000). This is important, as the leaching of metals from host rocks and their contained sulfide minerals can provide a source of metals for the overlying seafloor hydrothermal deposits.

Pyrites from the seawater-influenced chlorite-rich overprinting alteration zones have a different trace metal content compared to pyrites in the pyrophyllite ± natroalunite alteration zones (Fig. 5 and 10). That is, Cu, Bi and Te are relatively depleted in pyrite from seawater alteration assemblages when compared to pyrite from the magmatic volatile assemblages. This provides evidence for the leaching and remobilization of Cu, Bi and Te during the overprinting of magmatic volatile alteration by seawater-derived hydrothermal fluid. Moreover, the total measured trace metal content of pyrite from seawater-influenced samples is the lowest measured in our dataset at 173 ppm, indicating that metals have been removed. The remobilization of metals from pyrite provides a potential source of metals for black smoker chimneys at the seafloor that are enriched in Cu (up to 28 wt.%) and contain Te and Bi-rich minerals such as tellurobismuthite (de Ronde et al. 2011; Berkenbosch et al. 2012). A depletion in Cu, Te and Bi in pyrite from overprinting chlorite + quartz alteration corroborates previous interpretations that suggest the remobilization of metals at the NW Caldera by late-stage seawater-derived hydrothermal fluids (de Ronde et al. 2019a). Moreover, if pyrite from chlorite + quartz alteration was solely precipitated during later seawater overprinting then it is expected to have higher $\delta^{34}S$ values (>0‰) due to the contribution of sulfur from TSR of seawater, and this is not the case.

Textural analysis of pyrite confirms that it did not undergo complete dissolution during fluid overprinting, instead undergoing metal leaching and recrystallization (Fig. 3K). Pyrite from the Upper Cone contains

sharp zonations that occur parallel to the grain margin (Fig. 4K and L), similar to those present in pyrite from near seafloor samples (30 mbsf) at the NW Caldera (Fig. 3J). In deeper chlorite-rich samples that have been overprinted, pyrite exhibits diffuse poorly defined zonations, relict crystal faces, inclusions of anhydrite, and regions of complex growth zonation that are often chaotic in nature (Fig. 3K). We suggest that these features form when aggregates of fine-grained pyrite such as those observed at the Upper Cone (Fig. 4H) undergo recrystallization leading to the preservation of relict grain boundaries as zonations within a now larger mineral grain (Fig. 3K). In addition to geochemical and isotopic evidence, the preservation of zonations with diffuse margins and complex recrystallization textures support the observation that pyrite did not undergo complete dissolution during seawater overprinting.

The distribution of trace metals with depth below the seafloor

At the NW Caldera site, Hole U1530A, the distribution of trace metals in pyrite from chlorite-rich alteration shows a pronounced change with depth below the seafloor. At the seafloor and to a depth of ~30 mbsf, As, Sb, Ag and Pb are strongly enriched in pyrite whilst metals that are associated with higher-temperature fluids (>300 °C) are strongly depleted, including Co, Te, Se and Bi - with all or most analyses below the detection limit for these elements (Fig. 6A). The suite of metals enriched in the uppermost 30 mbsf of Hole U1530A, in chlorite-rich alteration, is best explained by a high-degree of seawater influx that lowers fluid temperature leading to an enrichment in metals such as As, Ag and Pb that are stable in lower temperature fluids (<300 °C) (Tivey et al. 1995; Edmonds et al. 1996). Heat flow modelling and near-seafloor magnetic data indicate that ascending high-temperature (>300 °C) hydrothermal fluid did not undergo large amounts of cooling during mixing with seawater at the NW Caldera (Caratori Tontini et al. 2012; 2019). Hence As, Ag, Sb and Pb will remain in solution, precipitating near the seafloor (~30 mbsf) where seawater mixing during shallow recharge is high and the fluid temperature is lower.

Above 153 mbsf all the way to the seafloor at the Upper Cone site, Cu, Zn, Se, Sb, Ag, Te, Pb and Bi are enriched in pyrite relative to samples below this depth, which are slightly enriched in Co and As (Fig. 6B). It is unlikely that this difference relates to a sampling bias as samples from both above and below 153 mbsf

contain pyrite from all three alteration assemblages. Heat flow modelling and near seafloor magnetic data indicate that seawater recharge occurs through the flanks of the Upper Cone (Caratori-Tontini et al. 2012, 2019), lowering the temperature of the ascending hydrothermal fluid and enhancing metal precipitation efficiency, thus explaining the higher metal content of pyrite close to the seafloor (Edmonds et al. 1996; Metz and Trefry 2000).

Trace metal and sulfur cycling in a hydrothermally active arc volcano

The trace metal enrichment signature of sub-seafloor pyrite at Brothers is relatively homogenous between the different sites and alteration assemblages. However, trace metal contents exhibit some variation between pyrite associated with magmatic volatile influenced pyrophyllite + natroalunite alteration at the Upper Cone and NW Caldera (<189 mbsf) and those that have been overprinted by seawater-derived hydrothermal fluids represented by chlorite-rich alteration.

Pyrite analyzed from drill core from the Upper Cone (Hole U1528D) and pyrophyllite + illite alteration from the NW Caldera (Hole U1530A) exhibit the same metal enrichment signature; however the trace metal content of pyrite between the two sites differs slightly (Fig. 5A and B). Our data indicate that pyrite initially has a higher Cu, As, Sb, Pb and Pt content at the younger Upper Cone site with pyrite becoming progressively enriched in Co, Se, Te and Bi over time, which is observed in pyrite at the older NW Caldera site (Ditchburn and de Ronde 2017). The enrichment of Co, Se, Te and Bi relates to the prolonged exposure and recrystallization of older pyrite generations at the NW Caldera site (<189 mbsf; Ditchburn and de Ronde 2017) due to the influx of magmatic volatiles. We interpret the enrichment of Co to indicate higher formation temperatures, as Co is often enriched in high-temperature pyrite generations (>300 °C; Metz and Trefry 2000). This is in good agreement with the mineralogical observations from pyrophyllite + illite samples at the NW Caldera that contain diaspore and zunyite indicating temperatures in excess of ~320 °C, minerals that are absent at the Upper Cone, suggesting lower fluid:rock ratios and higher fluid temperatures at the NW Caldera (de Ronde et al. 2019b,c). In addition to changes in trace metal content with age, the size and morphology of pyrite grains also varies. Pyrite at the younger Upper Cone site is generally

511 euhedral, forms aggregates and is very fine-grained (<< 1 mm), whereas pyrite from the lower NW Caldera
512 is coarse-grained and subhedral to anhedral (Fig. 3 and 4). This indicates a change in pyrite morphology
513 with time due to recrystallization and in some cases, dissolution (Fig. 4L) related to prolonged exposure to
514 high-temperature oxidized fluids (Fig. 12).

515 The similarity in trace metal enrichment signatures and sulfur isotope ratios between pyrite in pyrophyllite
516 ± natroalunite alteration at the NW Caldera and Upper Cone with pyrite from overprinting chlorite + quartz-
517 rich alteration (Fig. 5) indicates that pyrite is largely preserved during fluid overprinting, explaining the
518 similar trace metal enrichment signature between all pyrite at Brothers. However, the relative depletion of
519 pyrite from chlorite + quartz alteration in Cu, Te and Bi compared with all other pyrite indicates the
520 remobilization of these metals during fluid overprinting at the NW Caldera and their subsequent deposition
521 in black smoker chimneys at the seafloor (Berkenbosch et al. 2012, 2019). Our study provides evidence of
522 metal remobilization from pyrite that, in addition to the scavenging of magmatic brines by seawater-derived
523 hydrothermal fluids, is an important process in the accumulation of metals in hydrothermal precipitates at
524 the seafloor at Brothers (de Ronde et al. 2019a). A later seawater overprint is absent at the Upper Cone,
525 hence pyrite remains relatively enriched in Cu, Te and Bi compared to pyrite associated with chlorite +
526 quartz alteration (Fig. 5A).

527 The enrichment of As, Sb, Ag, Pb and lower contents of Co, Se and Te in the shallow subsurface to ~30
528 mbsf in overprinting chlorite-rich alteration at the NW Caldera is best explained by seawater mixing during
529 shallow recharge, although phase separation of the hydrothermal fluid cannot be ruled out. The absence of
530 the same enrichment pattern with depth below the seafloor (Fig. 6) at the Upper Cone (Hole U1528D)
531 indicates that fluid mixing and seawater recharge occurs over a much broader zone, supporting previous
532 geophysical investigations that showed recharge of seawater through the Upper Cone walls and pit crater
533 (Caratori-Tontini et al. 2012). In contrast, at the NW Caldera, ascending magmatic-hydrothermal fluid only
534 undergoes high-degrees of mixing and cooling within ~30 m of the seafloor, causing a pronounced change
535 in fluid temperature and the deposition of pyrite with a high As, Sb, Ag and Pb content.

Implications for formation of VMS and epithermal deposits

Data collected from below the seafloor at Brothers volcano offers a rare glimpse into subsurface processes in an active seafloor hydrothermal system. Brothers provides an analogue characterizing the transition between two major ore forming environments: volcanogenic massive sulfide (VMS) and high-sulfidation epithermal Au deposits (Sillitoe et al. 1996). At both the NW Caldera and Upper Cone sites metal enrichment below the seafloor is minimal, and only rarely were sulfide minerals other than pyrite observed. The low trace metal content of pyrite and absence of chalcopyrite and sphalerite, which are common in hydrothermal precipitates at the seafloor (Hannington et al. 2005), shows that mineralization containing high metal contents (i.e. several wt.% Zn or Cu), at least in the case of Brothers, is limited to a thin veneer at or near the seafloor, with sphalerite only commonly observed up to 30 mbsf. This shows that the potential to form economic mineralization below the seafloor is limited in both immature epithermal-type environments such as the Upper Cone and seawater-influenced systems like the NW Caldera. However, deposits that display transitional characteristics between seawater and magmatic-influenced systems, containing both pyrophyllite-rich and chlorite-rich alteration are prospective for mineral exploration due to the remobilization of metals from magmatic brines and overprinting of early pyrite generations that ultimately lead to the formation of metal-rich hydrothermal precipitates at the seafloor. Similar advanced-argillic alteration mineral assemblages have been documented in VMS deposits (Huston et al. 2011) such as LaRonde Penna (Canada; Mercier-Langevin et al. 2007), Mount Lyell (Tasmania; Large et al. 1996) and Boliden (Sweden; Mercier-Langevin et al. 2013). Understanding the transition from magmatic to seawater-influenced hydrothermal systems is important as LaRonde Penna, Mount Lyell and Boliden are all enriched in Au and classified as auriferous (Mercier-Langevin et al. 2011). The enrichment of Au in these deposits and associated advanced argillic alteration assemblage is attributed to the contribution of magmatic volatiles (Huston et al. 2011), hence characterizing the transition from magmatic to seawater-dominated hydrothermal systems is important for understanding the enrichment of Au in VMS deposits.

Summary and Conclusions

The combination of sulfur isotope and trace metal analysis of pyrite from below the seafloor at Brothers volcano shows variation with depth below the seafloor and between the NW Caldera and Upper Cone sites. Most trace metals occur in low concentrations and are incorporated in pyrite as a lattice bound substitution, with the exception of Zn, and more rarely Cu, which are hosted as micro-inclusions of sphalerite and chalcopyrite. Initially pyrite at the Upper Cone is enriched in Cu, As, Sb, Pb and Pt compared with older pyrite from pyrophyllite + illite alteration in the lower portion of the NW Caldera (<189 mbsf), which has a higher Cu, Te, Se and Bi content. This indicates a change in the trace metal content of pyrite with the age of the hydrothermal system related to higher fluid temperatures and prolonged exposure to magmatic volatile degassing.

The sulfur isotopic composition ($\delta^{34}S$) of pyrite supports previous interpretations that disproportionation of degassing SO_2 is a major source of sulfur in the Brothers hydrothermal system(s). In addition to SO_2 disproportionation, the occurrence of several values that are >0‰ at the NW Caldera indicates an additional source of sulfur, from TSR of seawater and leaching of host rocks. In combination, the uniform $\delta^{34}S$ composition and trace metal enrichment signature of pyrite across all alteration types indicate that pyrite did not undergo complete dissolution during seawater overprinting, although Cu, Te and Bi were remobilized by this process. These metals are then enriched in metal-sulfide-rich chimneys on the seafloor at the NW Caldera, further supporting the critical role of seawater-derived hydrothermal fluids in the formation of metal-rich hydrothermal precipitates at the seafloor.

Acknowledgments

This research used samples and data provided by the International Ocean Discovery Program (IODP). We thank the captain, crew and technical staff aboard the D/V *JOIDES Resolution* during Expedition 376 "Brothers Arc Flux", May-July 5th, 2018. AJM acknowledges the support of the European Consortium for Ocean Research Drilling during his participation on Expedition 376. Post-cruise research was funded by

584 the Natural Environmental Research Council grant NE/S006214/1 awarded to CJM and AJM at Cardiff
585 University. JWJ acknowledges support from the Canada Research Chair program. CdR acknowledges
586 funding from the Ministry of Business, Innovation and Employment of the New Zealand Government. We
587 thank S. Tombros and an anonymous reviewer for their valuable feedback and associate editor D. Zhai and
588 editor-in-chief G. Beaudoin for the editorial handling of this manuscript.

589 Author contributions

590 AJM was responsible for the study conception and design. Material preparation, data collection and analysis
591 were performed by AJM, GP and IMD. The first draft of the manuscript was written by AJM and all authors
592 commented on previous versions of the manuscript. All authors read and approved the final manuscript.

593 References

594 Abraitis PK, Pattrick RAD, Vaughan DJ (2004) Variations in the compositional, textural and electrical
595 properties of natural pyrite: a review. International Journal of Mineral Processing 74, 41–59.
596 Baker ET, Walker SL, Embley RW, de Ronde CEJ (2012) High-Resolution Hydrothermal Mapping of
597 Brothers Caldera, Kermadec Arc. Econ Geol 107:1583–1593
598 Banerjee NR, Gillis KM, Muehlenbachs K (2000) Discovery of epidosites in a modern oceanic setting,
599 the Tonga forearc. Geology 28:151-154
600 Berkenbosch HA, de Ronde CEJ, Ryan CG, McNeill AW, Howard DL, Gemmell JB, Danyushevsky LV
601 (2019) Trace Element Mapping of Copper- and Zinc-Rich Black Smoker Chimneys from
602 Brothers Volcano, Kermadec Arc, Using Synchrotron Radiation XFM and LA-ICP-MS. Econ
603 Geol 114:67–92
604 Berkenbosch HA, de Ronde CEJ, Gemmell JB, McNeill AW, Goemann K (2012) Mineralogy and
605 Formation of Black Smoker Chimneys from Brothers Submarine Volcano, Kermadec Arc. Econ
606 Geol 107:1613–1633

607 Binns RA, Barriga FJAS, Miller DJ, et al. (2002) *in* Binns RA. et al. eds., Initial report summary, Leg
608 193 Proceedings of the International Ocean Discovery Program: College Station, Texas,
609 International Ocean Discovery Program, pp. 84
610 Brueckner SM, Piercey SJ, Layne GD, Piercey G, Sylvester PJ (2015) Variations of sulphur isotope
611 signatures in sulphides from the metamorphosed Ming Cu(−Au) volcanogenic massive sulphide
612 deposit, Newfoundland Appalachians, Canada. Miner Deposita 50:619–640
613 Butler IB, Nesbitt RW (1999) Trace element distributions in the chalcopyrite wall of a black smoker
614 chimney: insights from laser ablation inductively coupled plasma mass spectrometry (LA–ICP–
615 MS). Earth Planet Sci Lett 167:335–345
616 Butterfield DA, Nakamura K, Takano B, Lilley MD, Lupton JE, Resing JA, Roe KK (2011) High SO2
617 flux, sulfur accumulation, and gas fractionation at an erupting submarine volcano. Geology 39:
618 803–806
619 Caratori Tontini F, Tivey MA, de Ronde CEJ, Humphris SE (2019) Heat Flow and Near-Seafloor
620 Magnetic Anomalies Highlight Hydrothermal Circulation at Brothers Volcano Caldera, Southern
621 Kermadec Arc, New Zealand. Geophys Res Lett 46:8252–8260
622 Caratori Tontini F, de Ronde CEJ, Yoerger D, Kinsey J, Tivey M (2012) 3-D focused inversion of near-
623 seafloor magnetic data with application to the Brothers volcano hydrothermal system, Southern
624 Pacific Ocean, New Zealand. J Geophys Res Solid Earth 117:B10102
625 Cook NJ, Ciobanu CL, Pring A, Skinner W, Shimizu M, Danyushevsky L, Saini-Eidukat B, Melcher F
626 (2009) Trace and minor elements in sphalerite: A LA-ICPMS study. Geochim Cosmochim Acta
627 73:4761–4791
628 de Ronde CEJ, Butterfield DA, Leybourne MI (2012) Metallogenesis and Mineralization of Intraoceanic
629 Arcs I: Kermadec Arc—Introduction. Econ Geol p.107:1521–1525
630 de Ronde CEJ, Faure K, Bray CJ, Chappell DA, Wright IC (2003) Hydrothermal fluids associated with
631 seafloor mineralization at two southern Kermadec arc volcanoes, offshore New Zealand. Miner
632 Deposita 38:217–233

633 de Ronde CEJ, Chadwick WW, Ditchburn RG, Embley RW, Tunnicliffe V, Baker ET, Walker SL, Ferrini
634 VL, Merle SM (2015) Molten Sulfur Lakes of Intraoceanic Arc Volcanoes, in: Rouwet, D.,
635 Christenson, B., Tassi, F., Vandemeulebrouck, J. (Eds.), Volcanic Lakes, Advances in
636 Volcanology. Springer, Berlin, Heidelberg, pp. 261–288
637 de Ronde CEJ, Massoth GJ, Butterfield DA, Christenson BW, Ishibashi J, Ditchburn RG, Hannington
638 MD, Brathwaite RL, Lupton JE, Kamenetsky VS, Graham IJ, Zellmer GF, Dziak RP, Embley
639 RW, Dekov VM, Munnik F, Lahr J, Evans LJ, Takai K (2011) Submarine hydrothermal activity
640 and gold-rich mineralization at Brothers Volcano, Kermadec Arc, New Zealand. Miner Deposita
641 46:541–584
642 de Ronde CEJ, Hannington MD, Stoffers P, Wright IC, Ditchburn RG, Reyes AG, Baker ET, Massoth
643 GJ, Lupton JE, Walker SL, Greene RR, Soong CWR, Ishibashi J, Lebon GT, Bray CJ, Resing JA
644 (2005) Evolution of a Submarine Magmatic-Hydrothermal System: Brothers Volcano, Southern
645 Kermadec Arc, New Zealand. Econ Geol 100:1097–1133
646 de Ronde CEJ, Humphris SE, Höfig TW, Reyes AG (2019a) Critical role of caldera collapse in the
647 formation of seafloor mineralization: The case of Brothers volcano. Geology 47:762–766
648 de Ronde CEJ, Humphris SE, Höfig TW, and the Expedition 376 Scientists (2019b) Site U1528, *in*
649 de Ronde CEJ, et al. (ed.), Brothers Arc Flux: Proceedings of the International Ocean
650 Discovery Program, Volume 376: College Station, Texas, International Ocean Discovery
651 Program, 66 p.
652 de Ronde CEJ, Humphris SE, Höfig TW, and the Expedition 376 Scientists (2019b) Site U1530, *in*
653 de Ronde CEJ, et al. (ed.), Brothers Arc Flux: Proceedings of the International Ocean
654 Discovery Program, Volume 376: College Station, Texas, International Ocean Discovery
655 Program, 53 p.

656 Deditius AP, Reich M, Kesler SE, Utsunomiya S, Chryssoulis SL, Walshe J, Ewing RC (2014) The
657 coupled geochemistry of Au and As in pyrite from hydrothermal ore deposits. Geochim
658 Cosmochim Acta 140:644–670
659 Deditius AP, Utsunomiya S, Reich M, Kesler SE, Ewing RC, Hough R, Walshe J (2011) Trace metal
660 nanoparticles in pyrite. Ore Geol Rev 42:32–46
661 Diehl A, de Ronde CEJ, Bach W (2020) Subcritical Phase Separation and Occurrence of Deep-Seated
662 Brines at the NW Caldera Vent Field, Brothers Volcano: Evidence from Fluid Inclusions in
663 Hydrothermal Precipitates. Geofluids 8868259
664 Ditchburn RG, de Ronde CEJ (2017) Evidence for Remobilization of Barite Affecting Radiometric
665 Dating Using 228Ra, 228Th, and 226Ra/Ba Values: Implications for the Evolution of Sea-Floor
666 Volcanogenic Massive Sulfides. Econ Geol 112:1231–1245
667 Edmonds HN, German CR, Green DRH, Huh Y, Gamo T, Edmond JM (1996) Continuation of the
668 hydrothermal fluid chemistry time series at TAG, and the effects of ODP drilling. Geophys Resh
669 Lett 23:3487–3489
670 Edmonds M, Wallace PJ (2017) Volatiles and Exsolved Vapor in Volcanic Systems. Elements 13:29–34
671 Embley RW, de Ronde CEJ, Merle SG, Davy B, Caratori Tontini F (2012) Detailed Morphology and
672 Structure of an Active Submarine Arc Caldera: Brothers Volcano, Kermadec Arc. Econ Geol
673 107:1557–1570.
674 Fuchs S, Hannington MD, Petersen S (2019) Divining gold in seafloor polymetallic massive sulfide
675 systems. Miner Deposita 54:789–820
676 Fouquet Y, Zierenberg RA, Miller DJ and Leg 169 Scientists (1998). , Fouquet et al. (ed.), Initial reports
677 of the Ocean Drilling Program, Leg 169: College Station, Texas, Ocean Drilling Program, p. 205-
678 252

679 Gemmell JB, Sharpe R, Jonasson IR, Herzig PM (2004) Sulfur Isotope Evidence for Magmatic
680 Contributions to Submarine and Subaerial Gold Mineralization: Conical Seamount and the
681 Ladolam Gold Deposit, Papua New Guinea. Econ Geol 99:1711–1725
682 George LL, Cook NJ, Ciobanu CL (2016) Partitioning of trace elements in co-crystallized sphalerite–
683 galena–chalcopyrite hydrothermal ores. Ore Geol Rev 77:97–116
684 Giggenbach WF (1996) Chemical Composition of Volcanic Gases, in: Scarpa, R., Tilling, R.I. (Eds.),
685 Monitoring and Mitigation of Volcano Hazards. Springer, Berlin, Heidelberg, pp. 221–256
686 Goldschmidt VM, Muir A (1954) Geochemistry. Clarendon Press, Oxford, p. 730
687 Grant HLJ, Hannington MD, Petersen S, Frische M, Fuchs SH (2018) Constraints on the behavior of trace
688 elements in the actively-forming TAG deposit, Mid-Atlantic Ridge, based on LA-ICP-MS
689 analyses of pyrite. Chem Geol 498:45–71
690 Gruen G, Weis P, Driesner T, Heinrich CA, de Ronde CEJ (2014) Hydrologic controls on
691 different styles of magmatic-hydrothermal activity with implications for ore deposit formation at
692 submarine arc volcanoes. Earth Planet Sci Lett 404:307-318
693 Haase KM, Stroncik N, Garbe-Schönberg D, Stoffers P (2006) Formation of island arc dacite magmas by
694 extreme crystal fractionation: An example from Brothers Seamount, Kermadec island arc (SW
695 Pacific). J Volcanol Geotherm Res 152, 316-330
696 Hannington MD, Tivey MK, Larocque ACL, Petersen S, Rona PA (1995) The occurrence of gold in
697 sulfide deposits of the TAG hydrothermal field, Mid-Atlantic Ridge. Canad Mineral33:1285–
698 1310
699 Hannington MD, de Ronde CEJ, Petersen S (2005) Sea-floor tectonics and submarine hydrothermal
700 systems, in: Hedenquist, J.W., Thompson, J.F.H., Goldfarb, R.J., Richards, J.P. (ed.), Economic
701 Geology 100th Anniversary Volume. Society of Economic Geologists, Littelton, Colorado, USA,
702 pp. 111–141

Hedenquist JW, Lowenstern JB (1994) The role of magmas in the formation of hydrothermal ore deposits. Nature 370:519–527

Herzig PM, Hannington MD, Arribas A (1998) Sulfur isotopic composition of hydrothermal precipitates from the Lau back-arc: implications for magmatic contributions to seafloor hydrothermal systems. Miner Deposita 33:226–237

Humphris SE, Herzig P, Miller D (1996) Introduction and principal results, in Humphris SE, et al. (ed.) Proceeding of the Ocean Drilling Program Initial Reports, Volume 158: College Station, Texas, International Ocean Discovery Program, 14 p.

Humphris SE, Herzig PM, Miller DJ, Alt JC, Becker K, Brown D, Brügmann G, Chiba H, Fouquet Y, Gemmell JB, Guerin G, Hannington MD, Holm NG, Honnorez JJ, Iturrino GJ, Knott R, Ludwig R, Nakamura K, Petersen S, Reysenbach A-L, Rona PA, Smith AAS, Tivey MK, Zhao X (1995) The internal structure of an active sea-floor massive sulphide deposit. Nature 377:713–716

Humphris SE, Thompson G (1978) Trace element mobility during hydrothermal alteration of oceanic basalts. Geoch Cosmochim Acta 42:127–136

Huston DL, Relvas JMRS, Gemmell JB, Drieberg S (2011) The role of granites in volcanic-hosted massive sulphide ore-forming systems: an assessment of magmatic–hydrothermal contributions. Miner Deposita 46:473–507

Huston DL, Sie SH, Suter GF, Cooke DR, Both RA (1995) Trace elements in sulfide minerals from eastern Australian volcanic-hosted massive sulfide deposits; Part I, Proton microprobe analyses of pyrite, chalcopyrite, and sphalerite, and Part II, Selenium levels in pyrite; comparison with delta 34 S values and implications for the source of sulfur in volcanogenic hydrothermal systems. Econ Geol 90:1167–1196

Keith M, Haase KM, Klemd R, Smith DJ, Schwarz-Schampera U, Bach W (2018b) Constraints on the source of Cu in a submarine magmatic-hydrothermal system, Brothers volcano, Kermadec island arc. Contrib Mineral Petrol 173-40:1-16

728 Keith M, Häckel F, Haase KM, Schwarz-Schampera U, Klemd R (2016) Trace element systematics of
729 pyrite from submarine hydrothermal vents. Ore Geol Rev 72:728–745
730 Keith M, Smith DJ, Jenkin GRT, Holwell DA, Dye MD (2018a) A review of Te and Se systematics in
731 hydrothermal pyrite from precious metal deposits: Insights into ore-forming processes. Ore Geol
732 Rev 96:269–282
733 Kleint C, Bach W, Diehl A, Fröhberg N, Garbe-Schönberg D, Hartmann JF, de Ronde CEJ, Sander SG,
734 Strauss H, Stucker VK, Thal J, Zitoun R, Koschinsky A (2019) Geochemical characterization of
735 highly diverse hydrothermal fluids from volcanic vent systems of the Kermadec intraoceanic arc.
736 Chem Geol 528:119289
737 Kusakabe M, Komoda Y, Takano B, Abiko T (2000) Sulfur isotopic effects in the disproportionation
738 reaction of sulfur dioxide in hydrothermal fluids: implications for the δ34S variations of dissolved
739 bisulfate and elemental sulfur from active crater lakes. J Volcanol Geotherm Res 97:287–307
740 Large RR (1992) Australian volcanic-hosted massive sulfide deposits: features, styles, and genetic
741 models. Econ Geol 87:471–510
742 Large RR, Danyushevsky L, Hollit C, Maslennikov V, Meffre S, Gilbert S, Bull S, Scott R, Emsbo P,
743 Thomas H, Singh B, Foster J (2009) Gold and Trace Element Zonation in Pyrite Using a Laser
744 Imaging Technique: Implications for the Timing of Gold in Orogenic and Carlin-Style Sediment-
745 Hosted Deposits. Econ Geol 104:635–668
746 Large RR, Doyle M, Raymond O, Cooke D, Jones A, Heasman L (1996) Evaluation of the role of
747 Cambrian granites in the genesis of world class VHMS deposits in Tasmania. Ore Geol Rev,
748 10:215-230
749 Layton-Matthews D, Leybourne MI, Peter JM, Scott SD, Cousens B, Eglington BM (2013) Multiple
750 sources of selenium in ancient seafloor hydrothermal systems: Compositional and Se, S, and Pb
751 isotopic evidence from volcanic-hosted and volcanic-sediment-hosted massive sulfide deposits of
752 the Finlayson Lake District, Yukon, Canada. Geochim Cosmochim Acta 117:313-331

753 Martin AJ, Keith M, Parvaz DB, McDonald I, Boyce AJ, McFall KA, Jenkin GRT, Strauss H, MacLeod
754 CJ (2020) Effects of magmatic volatile influx in mafic VMS hydrothermal systems: Evidence
755 from the Troodos ophiolite, Cyprus. Chem Geol 531:119325
756 Martin AJ, McDonald I, Jenkin GRT, McFall KA, Boyce AJ, Jamieson JW, MacLeod CJ (2021) A
757 missing link between ancient and active mafic-hosted seafloor hydrothermal systems – Magmatic
758 volatile influx in the exceptionally preserved Mala VMS deposit, Troodos, Cyprus. Chem Geol
759 567:120127
760 Martin AJ, Jamieson JW, de Ronde CEJ, Humphris SE, Roberts S, Macleod CJ, Cai Y, Zhang C, Schlicht
761 LEM, Nozaki T (2022). Hydrothermal alteration within the Brothers submarine arc volcano,
762 Kermadec arc, New Zealand. Econ Geol. https://doi.org/10.5382/econgeo.4962
763 Maslennikov VV, Maslennikova SP, Large RR, Danyushevsky LV (2009) Study of Trace Element
764 Zonation in Vent Chimneys from the Silurian Yaman-Kasy Volcanic-Hosted Massive Sulfide
765 Deposit (Southern Urals, Russia) Using Laser Ablation-Inductively Coupled Plasma Mass
766 Spectrometry (LA-ICPMS). Econ Geol 104:1111–1141
767 McDermott JM, Ono S, Tivey MK, Seewald JS, Shanks WC, Solow AR (2015) Identification of sulfur
768 sources and isotopic equilibria in submarine hot-springs using multiple sulfur isotopes. Geochim
769 Cosmochim Acta 160:169–187
770 Melekestseva IY, Tret'yakov GA, Nimis P, Yuminov AM, Maslennikov VV, Maslennikova SP,
771 Kotlyarov VA, Beltenev VE, Danyushevsky LV, Large RR (2014) Barite-rich massive sulfides
772 from the Semenov-1 hydrothermal field (Mid-Atlantic Ridge, 13°30.87′ N): Evidence for phase
773 separation and magmatic input. Mar Geol 349:37–54
774 Mercier-Langevin P, Dubé B, Hannington MD, Davis DW, Lafrance B, Gosselin G (2007) The LaRonde
775 Penna Au-Rich Volcanogenic Massive Sulfide Deposit, Abitibi Greenstone Belt, Quebec: Part I.
776 Geology and Geochronology. Econ Geol 102: 585–609
777 Mercier-Langevin P, Hannington MD, Dubé B, Bécu V (2011) The gold content of volcanogenic massive
778 sulfide deposits. Miner Deposita 46, 509–539

779 Mercier-Langevin P, McNicoll V, Allen RL, Blight JHS, Dubé B (2013) The Boliden gold-rich
780 volcanogenic massive sulfide deposit, Skellefte district, Sweden: new U–Pb age constraints and
781 implications at deposit and district scale. Miner Deposita 48, 485–504
782 Metz S, Trefry JH (2000) Chemical and mineralogical influences on concentrations of trace metals in
783 hydrothermal fluids. Geochim Cosmochim Acta 64:2267–2279
784 Monecke T, Petersen S, Hannington MD, Grant H, Samson I (2016) The minor element endowment of
785 modern sea-floor massive sulfide deposits and comparison with deposits hosted in ancient
786 volcanic successions, in: Verplanck, P.L., Hitzman, M.W. (ed.), Rare Earth and Critical Elements
787 in Ore Deposits. Society of Economic Geologists, Knoxville, Tenn., pp. 245–306
788 Nestmeyer M, Keith M, Haase KM, Klemd R, Voudouris P, Schwarz-Schampera U, Strauss H, Kati M,
789 Magganas A (2021) Trace Element Signatures in Pyrite and Marcasite From Shallow Marine
790 Island Arc-Related Hydrothermal Vents, Calypso Vents, New Zealand, and Paleochori Bay,
791 Greece. Front Earth Sci 9:138
792 Ohmoto H, Lasaga AC (1982) Kinetics of reactions between aqueous sulfates and sulfides in
793 hydrothermal systems. Geochim Cosmochim Acta 46:1727–1745
794 Ono S, Shanks WC, Rouxel OJ, Rumble D (2007) S-33 constraints on the seawater sulfate contribution in
795 modern seafloor hydrothermal vent sulfides. Geochim Cosmochim Acta 71:1170–1182
796 Patten CGC, Pitcairn IK, Alt JC, Zack T, Lahaye Y, Teagle DAH, Markdahl K (2020) Metal fluxes
797 during magmatic degassing in the oceanic crust: sulfide mineralisation at ODP site 786B, Izu-
798 Bonin forearc. Mineral Deposita 55:469–489
799 Peters C, Strauss H, Haase K, Bach W, de Ronde CEJ, Kleint C, Stucker V (2021) SO2
800 disproportionation impacting hydrothermal sulfur cycling: Insights from multiple sulfur isotopes
801 for hydrothermal fluids from the Tonga-Kermadec intraoceanic arc and the NE Lau Basin.
802 Chem Geol 120586.
803 Petersen S, Herzig PM, Hannington MD, Jonasson IR, Arribas A (2002) Submarine Gold Mineralization
804 Near Lihir Island, New Ireland Fore-Arc, Papua New Guinea. Economic Geology 97, 1795–1813.

805 Prichard HM, Knight RD, Fisher PC, McDonald I, Zhou MF, Wang CY (2013) Distribution of platinum-
806 group elements in magmatic and altered ores in the Jinchuan intrusion, China: an example of
807 selenium remobilization by postmagmatic fluids. Miner Deposita 48:767–786
808 Rahm M, Hoffmann R, Ashcroft NW (2016) Atomic and Ionic Radii of Elements 1–96. Chem Eur J 22:
809 14625–14632
810 Rees CE, Jenkins WJ, Monster J (1978) The sulphur isotopic composition of ocean water sulphate.
811 Geochim Cosmochim Acta 42:377–381
812 Reich M, Kesler SE, Utsunomiya S, Palenik CS, Chryssoulis SL, Ewing RC (2005). Solubility of gold in
813 arsenian pyrite. Geochim Cosmochim Acta 69:2781–2796
814 Reyes AG (1990) Petrology of Philippine geothermal systems and the application of alteration
815 mineralogy to their assessment. J Volcanol Geotherm Res 43:279–309
816 Richardson CJ, Cann JR, Richards HG, Cowan JG (1987) Metal-depleted root zones of the Troodos ore-
817 forming hydrothermal systems, Cyprus. Earth Plan Sci Lett 84:243–253
818 Ryan WBF, Carbotte SM, Coplan JO, O'Hara S, Melkonian A, Arko R, Weissel RA, Ferrini V, Goodwillie A,
819 Nitsche F, Bonczkowski J, Zemsky R (2009) Global Multi-Resolution Topography synthesis, Geochem
820 Geophys Geosyst 10:Q03014
821 Sakai H (1968) Isotopic properties of sulfur compounds in hydrothermal processes. Geochem J 2:29–49
822 Sakai H, Marais DJD, Ueda A, Moore JG (1984) Concentrations and isotope ratios of carbon, nitrogen
823 and sulfur in ocean-floor basalts. Geochim Cosmochim Acta 48:2433–2441
824 Sillitoe RH, Hannington MD, Thompson JFH (1996) High sulfidation deposits in the volcanogenic
825 massive sulfide environment. Econ Geol 91:204–212
826 Stucker VK, de Ronde CEJ, Laurence KJ, Phillips AM (2022) Rare Time Series of Hydrothermal Fluids
827 for a Submarine Volcano: 14 Years of Vent Fluid Compositions for Brothers Volcano, Kermadec
828 Arc New Zealand. Econ Geol https://doi.org/10.5382/econgeo.4922

829 Takai K, Mottl MJ, Nielsen SH and the Expedition 331 Scientists (2011) Proceedings of the International
830 Ocean Discovery Program, Volume 331: College Station, Texas, International Ocean Discovery
831 Program, p. 39

832 Timm C, de Ronde CEJ, Leybourne MI, Layton-Matthews D, Graham IJ (2012) Sources of Chalcophile
833 and Siderophile Elements in Kermadec Arc Lavas. Econ Geol 107:1527–1538

834 Tivey MK, Humphris SE, Thompson G, Hannington MD, Rona PA (1995) Deducing patterns of fluid
835 flow and mixing within the TAG active hydrothermal mound using mineralogical and
836 geochemical data. J Geophys Res: Solid Earth 100:12527–12555

837 Wallace PJ (2005) Volatiles in subduction zone magmas: concentrations and fluxes based on melt
838 inclusion and volcanic gas data. J Volcanol Geotherm Res 140:217–240

839 Wohlgemuth-Ueberwasser CC, Viljoen F, Petersen S, Vorster C (2015) Distribution and solubility limits
840 of trace elements in hydrothermal black smoker sulfides: An in-situ LA-ICP-MS study. Geochim
841 Cosmochim Acta 159:16–41

842 Wright IC, Gamble JA (1999) Southern Kermadec submarine caldera arc volcanoes (SW Pacific): caldera
843 formation by effusive and pyroclastic eruption. Mar Geol 161:207–227

844 Wysoczanski RJ, Handler MR, Schipper CI, Leybourne MI, Creech J, Rotella MD, Nichols ARL, Wilson
845 CJN, Stewart RB (2012) The Tectonomagmatic Source of Ore Metals and Volatile Elements in
846 the Southern Kermadec Arc. Econ Geol 107:1539–1556

847 Yang K, Scott SD (2002) Magmatic Degassing of Volatiles and Ore Metals into a Hydrothermal System
848 on the Modern Sea Floor of the Eastern Manus Back-Arc Basin, Western Pacific. Econ Geol 97:
849 1079–1100

850 Yang K, Scott SD (1996) Possible contribution of a metal-rich magmatic fluid to a sea-floor hydrothermal
851 system. Nature 383:420–423

852 Yeats CJ, Parr JM, Binns RA, Gemmell JB, Scott SD (2014) The SuSu Knolls Hydrothermal Field,
853 Eastern Manus Basin, Papua New Guinea: An Active Submarine High-Sulfidation Copper-Gold
854 System. Econ Geol 109:2207–2226
855 Zeng Z, Liu C, Chen CA, Yin X, Chen D, Wang XY, Wang X, Zhang G (2007) Origin of a native sulfur
856 chimney in the Kueishantao hydrothermal field, offshore northeast Taiwan. Sci China Earth Sci
857 50:1746-1753

858 Figure Captions

859 Figure 1: Location map of Kermadec-Tonga arc and surrounding area. Brothers volcano is located on the
860 southern Kermadec arc, NE of New Zealand (data: http://www.geomapapp.org; Ryan et al. 2009)

861 Figure 2: Bathymetric map of Brothers volcano. A) Approximate location of drill sites investigated in this
862 study. Hole U1530A is located at the NW Caldera site and Hole U1528D is located at the Upper Cone
863 (legend as in image B). B) 3D visualization of Brothers caldera looking approximately NE, note that the
864 bathymetry is exaggerated by 2 times (data: GNS Science).

865 Figure 3: Representative photographs of drill core sections and photomicrographs of pyrite in reflected light
866 from the NW Caldera site. A-1) Core recovery (black lines) and the distribution of different alteration
867 mineral assemblages with depth below the seafloor (green = chlorite-rich, red = pyrophyllite-rich). A)
868 Stockwork veins from 26 mbsf containing pyrite + barite + anhydrite ± sphalerite (core section 5R1, 25.9
869 mbsf). Clast material consists of smectite + chlorite + quartz. B) Brecciated sample (core section 13R1,
870 64.3 mbsf) containing chlorite + quartz altered clasts with a matrix of pyrite + quartz + anhydrite. C)
871 Representative sample of pyrophyllite + illite alteration (core section 48R1, 232.3 mbsf). Light coloured
872 regions are quartz + anhydrite-rich whereas buff-beige areas are illite + pyrophyllite-rich. D) Anhydrite +
873 pyrite vein containing coarse subhedral-to-euhedral pyrite (core section 1R1, 0.3 mbsf). E) Subhedral to
874 euhedral pyrite from chlorite + quartz alteration zone (core section 69R1, 333.2 mbsf). F) Fine-grained
875 euhedral pyrite aggregates in a matrix of chlorite + quartz (core section 5R1, 25.9 mbsf). G) Pyrite in

pyrophyllite + illite alteration associated with a late, cross-cutting anhydrite vein (core section 44R1, 214.0 mbsf). H) Subhedral pyrite grains with abundant sphalerite inclusions (inset image) from pyrophyllite + illite alteration zone (core section 65R1, 314.4 mbsf). I) Anhedral, resorbed pyrite from pyrophyllite + illite alteration zone (core section 69R1, 333.2 mbsf). J) Euhedral pyrite with radial zonations delineating multiple generations of overgrowth (core section 1R1, 0.3 mbsf). K) Subhedral pyrite from chlorite + quartz alteration with weak zonation and a relict core "C" indicating recrystallization. White dashed lines delineate relict crystal faces (core section 89R1, 429. 5 mbsf). Inset image provides a close up view of an area with chaotic zonations with grain boundaries delineated by brighter orange colors. L) Anhedral pyrite with radial zonations that are subparallel to the grain margin showing a prominent relict core "C" zone (core section 65R1, 314.4 mbsf). Images J to L have been etched for 90 s with NaOCl. Sample intervals and depths in ESM 1, Table T2.

Figure 4: Representative photographs of drill sections and photomicrographs of pyrite grains in reflected light from the Upper Cone site. A-1) Core recovery (black lines) and the distribution of different alteration mineral assemblages with depth below the seafloor (blue = smectite-rich, pink = natroalunite + pyrophyllite-rich, orange = natrolaunite-rich). A) Natroalunite bearing alteration containing bleached selvages (white material) with native sulfur (Nat S) infilling porosity (core section 18R2, 138.9 mbsf). B) Natroalunite + pyrophyllite alteration with a prominent brecciated texture; clasts (C) are variably altered with their rim often appearing more altered than the core (core section 9R1, 95.1 mbsf). C) Smectite-rich alteration containing primary plagioclase (core section 37R1, 229.7 mbsf). D) Fine-grained subhedral to euhedral pyrite in a matrix of pyrophyllite + quartz (core section 6R1, 85.6 mbsf). E) Pyrite associated with a cross-cutting anhydrite veinlet (core section 5R2, 77.6 mbsf). F) Pyrite surrounding a plagioclase glomerocryst that has been replaced by natroalunite + anhydrite (core section 55R1, 316.7 mbsf). G) Pyrite associated with anhydrite that has replaced a plagioclase + pyroxene glomerocryst (core section 14R1, 120.2 mbsf). H) An aggregate of euhedral pyrite infilling porosity (core section 11R3, 104.9 mbsf). I) Fine-grained euhedral pyrite associated with secondary Ti minerals (core section 9R1, 95.4 mbsf). J) Euhedral

to subhedral pyrite with sub-grains with no internal zonation (core section, 5R1 75.7 mbsf). K) An aggregate of very fine-grained pyrite with some grains exhibiting radial zonation (core section 11R3, 104.9 mbsf). L) Very fine-grained pyrite exhibiting parallel zonation and an inclusion-rich core (core section 38R1, 234.5 mbsf). Images J to L have been etched for 90 s with NaOCl. Sample intervals available in ESM 1, Table T2.

Figure 5: Trace metal geochemistry of pyrite (LA-ICP-MS) classified by alteration mineralogy. A) Comparison of the median concentration of trace metals in pyrite from natroalunite (N-alun, *n= 37 spots*), natroalunite + pyrophyllite (N-alun + prl, *n= 151 spots*), smectite + plagioclase (smec + plag, *n= 28 spots*), pyrophyllite + illite (prl + ill, *n= 76 spots*) and chlorite + quartz (chl + qtz, *n=53 spots*) alteration. The grey line represents the median trace metal content for all pyrite and the surrounding grey area is the interquartile range. All pyrite exhibits broadly the same trace metal signature but the absolute abundance of different metals varies, notably pyrite from chlorite + quartz alteration is relatively depleted in Cu, Te and Bi. B) Cu, C) Zn, D) Pb, E) Co, F) As, G) Se, H) Te, I) Sb, J) Ag, K) Pt, L) Au, M) Bi.

Figure 6: Variation in downhole trace metal contents of pyrite from A) the NW Caldera site and B) the Upper Cone site for Co, Cu, Se, Te, Bi, Sb, Pb, As and Ag. In Hole U1530A at the NW Caldera site, Sb, Pb, As and Ag are enriched near the seafloor in chlorite-rich alteration. In Hole U1528D at the Upper Cone site, most trace metals are enriched in samples above 153 mbsf relative to deeper samples. Black dots represent the median trace metal content of a given sample and error bars span the minimum and maximum contents.

Figure 7: Sulfur isotope composition ($\delta^{34}S$) of pyrite from the NW Caldera (red and green) and Upper Cone (orange, pink blue) sites, classified by alteration mineralogy (N-alun *n= 8*, N-alun + prl, *n= 16*, Smec + plag *n= 7*, Prl + ill *n= 20*, chl + qtz *n=* 27). The median $\delta^{34}S$ value for all alteration types is similar. Data available in ESM 1, Table T7.

924 Figure 8: Downhole variations in the sulfur isotope composition ($\delta^{34}S$) of pyrite. A) Average $\delta^{34}S$ values in
925 pyrite from Hole U1530A of the NW Caldera (*n= 46 points,* 14 samples). B) Average $\delta^{34}S$ values in pyrite
926 from Hole U1528D of the Upper Cone site (*n= 32 points*, 13 samples). Error bars represent minimum and
927 maximum value for a given sample. Vent fluid HS^- (de Ronde et al. 2011) and arc-enriched mantle
928 (McDermott et al. 2015).

929 Figure 9: Representative time resolved analysis (TRA) (LA-ICP-MS) for pyrite (counts per second vs.
930 time). A smooth ablation profile indicates the incorporation of trace metals in a solid solution, or as nano-
931 scale inclusions, whereas a jagged profile typically indicates mineral inclusions (note logarithmic scale).
932 A) Pyrite from core section 52R2 (301.7 mbsf, Hole U1528D). B) Pyrite from core section 29R2 (191.3
933 mbsf, Hole U1528D) contains inclusions of probable sphalerite (sph) and chalcopyrite (ccp). Grey box
934 marks gas blank measurement. Red arrow = laser off.

935 Figure 10: Geochemical discrimination diagrams for pyrite geochemistry. Data from this study are indicated
936 by the colored symbols and are classified based on alteration mineralogy. Gray symbols are the LA-ICP-
937 MS analysis of pyrite from other seafloor massive sulfide deposits. A) Au vs. As. The black dashed line
938 marks the solubility limit of Au in pyrite as a function of As concentration. Concentrations below the solid
939 black dashed line are considered to be hosted in a lattice bound solid solution whereas values above indicate
940 inclusions (after Reich et al. 2005). B) Te vs. As. The black dashed line indicates the maximum solubility
941 of Te as a function of As concentration. Points that plot above the line indicate the occurrence of inclusions
942 (after Keith et al. 2018a). C) Sb vs. As, samples from the NW Caldera site are notably enriched in Sb and
943 As. D) Boiling discrimination plot using the ratio of Sb/Pb and Bi/Pb (after Román et al. 2019). All data in
944 ppm. Gray symbols are the LA-ICP-MS analysis of pyrite from other seafloor massive sulfide deposits (de
945 Ronde et al. 2011 – whole rock data; Wohlgemuth-Ueberwasser et al. 2015; Keith et al. 2016; Grant et al.
946 2018).

Figure 11: Summary of sulfur isotope composition of sulfide minerals from Brothers. The average $\delta^{34}S$ composition of sulfide minerals, native sulfur and vent fluid HS (data from de Ronde et al. 2003, 2005, 2011).

Figure 12: Summary of pyrite evolution, trace metal enrichment signatures and sulfur isotope composition of sub-seafloor pyrite at the Brothers volcano. A) Pyrite forming at the Upper Cone site. Pyrite is fine-grained, euhedral and enriched in Cu, As, Sb and Pb. Disproportionation of degassing SO_2 is the primary source of sulfur. B) Pyrite from pyrophyllite + illite alteration at the NW Caldera. Pyrite becomes progressively coarser due to recrystallization with time and is relatively enriched in Co, Se, Te and Bi with a subhedral grain morphology. Cobalt, Se, Te and Bi are progressively enriched due to prolonged periods of magmatic volatile degassing at high-temperature (>300 °C). C) Seawater-derived hydrothermal overprinting of pyrophyllite + illite alteration and the formation of chlorite + quartz alteration at the NW Caldera. Hydrothermal fluids remobilize Cu, Te and Bi from pyrite but the trace metal enrichment signature and $\delta^{34}S$ value remains unchanged, indicating that pyrite did not undergo complete dissolution during fluid overprinting.

Table Captions

Table 1: Summary of pyrite trace metal contents from the NW Caldera and Upper Cone site, classified by alteration mineral assemblage. Av. = average, med. = median, σ = one standard deviation, max = maximum. Chl + qtz = chlorite + quartz, Prl + ill = pyrophyllite + illite, Smec + plg = smectite + plagioclase, N-alu + prl = natroalunite + pyrophyllite, N-alu = natrolaunite (ESM 1, Table T4 and 5).

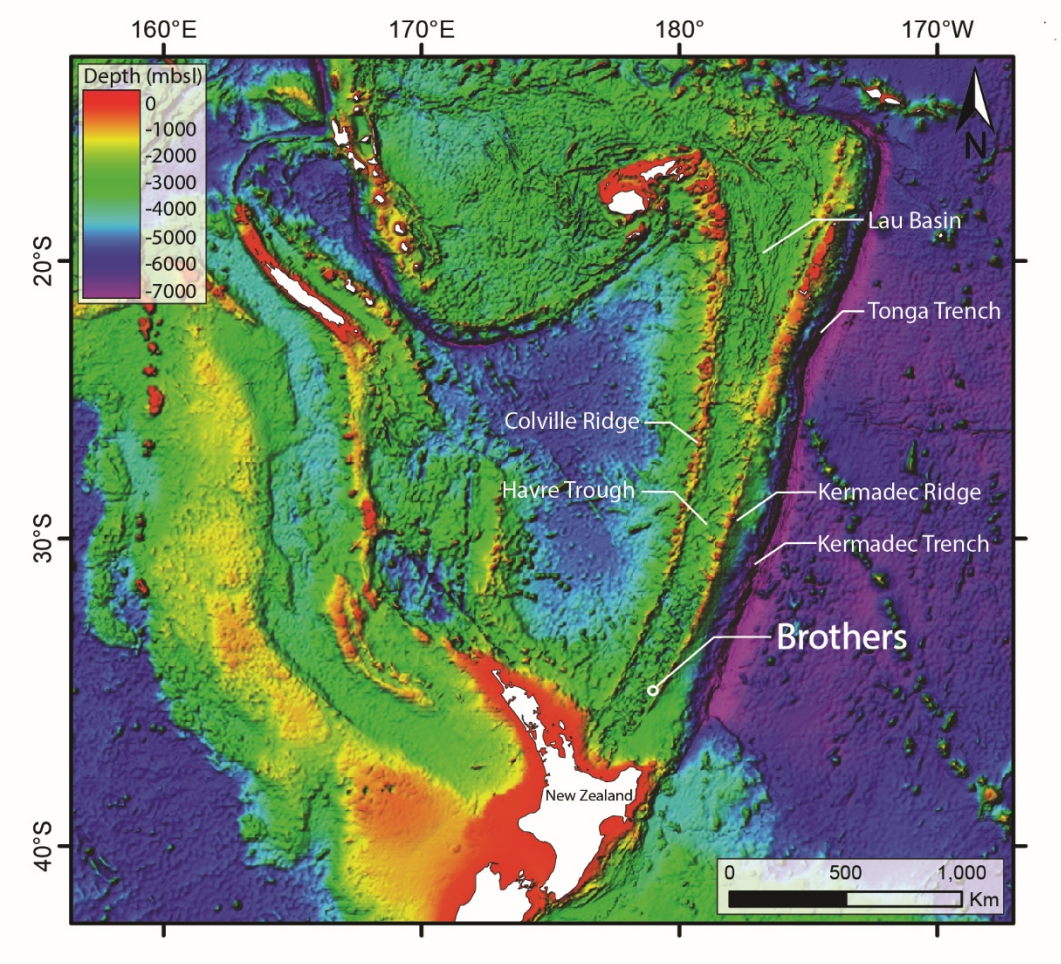
160°E
170°E
180°
170°W
20°S
30°S
40°S
Depth (mbsl)
0
-1000
-2000
-3000
-4000
-5000
-6000
-7000
N
Lau Basin
Tonga Trench
Colville Ridge
Havre Trough
Kermadec Ridge
Kermadec Trench
Brothers
New Zealand
0
500
1,000
Km

987

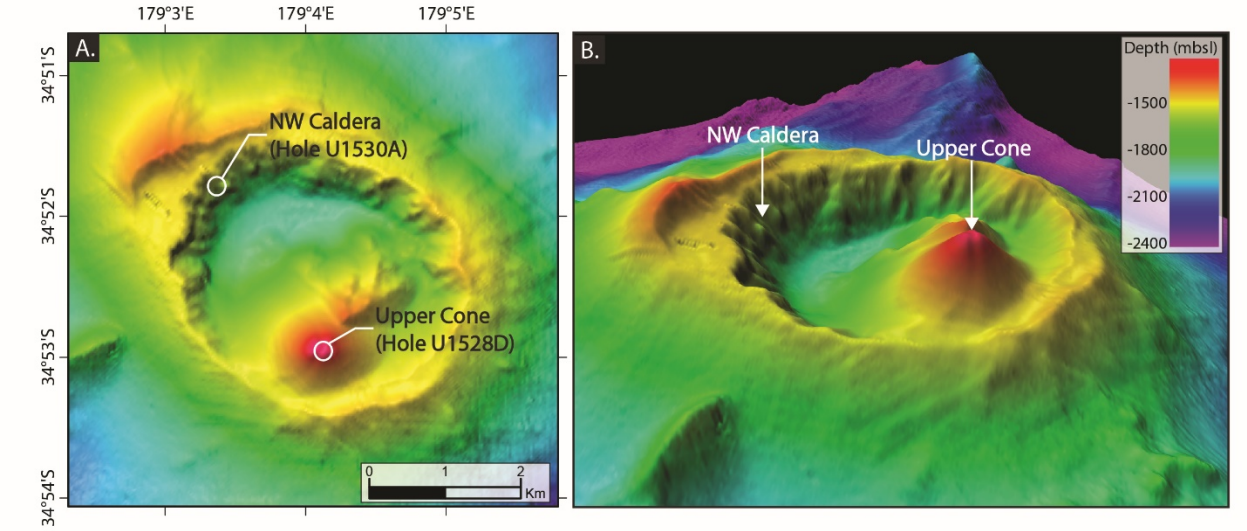
179°3'E
179°4'E
179°5'E
34°51'S
34°52'S
34°53'S
34°54'S
A.
NW Caldera
(Hole U1530A)
Upper Cone
(Hole U1528D)
0
1
2
Km
B.
NW Caldera
Upper Cone
Depth (mbsl)
-1500
-1800
-2100
-2400

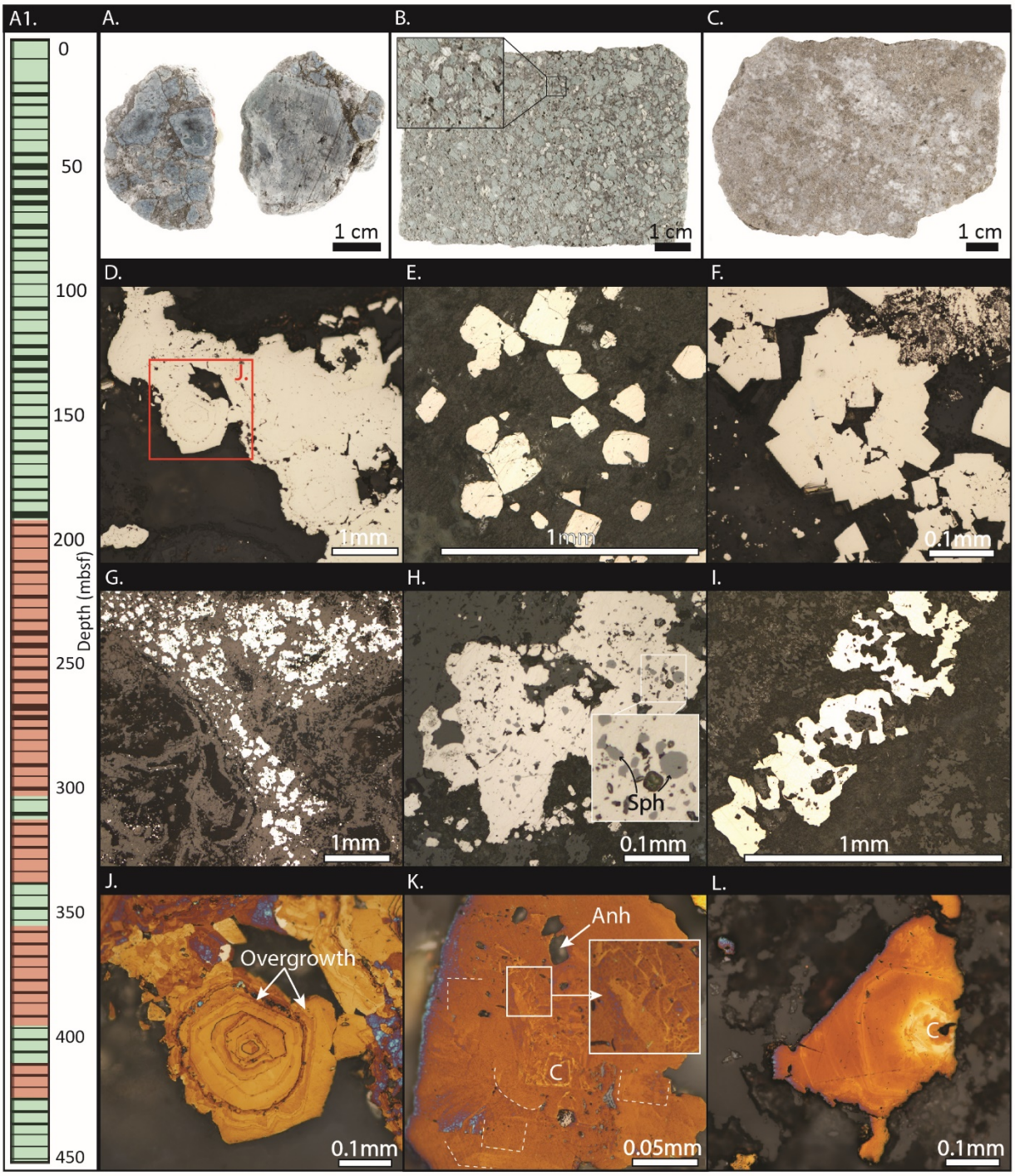

1019

1020

1021

1022

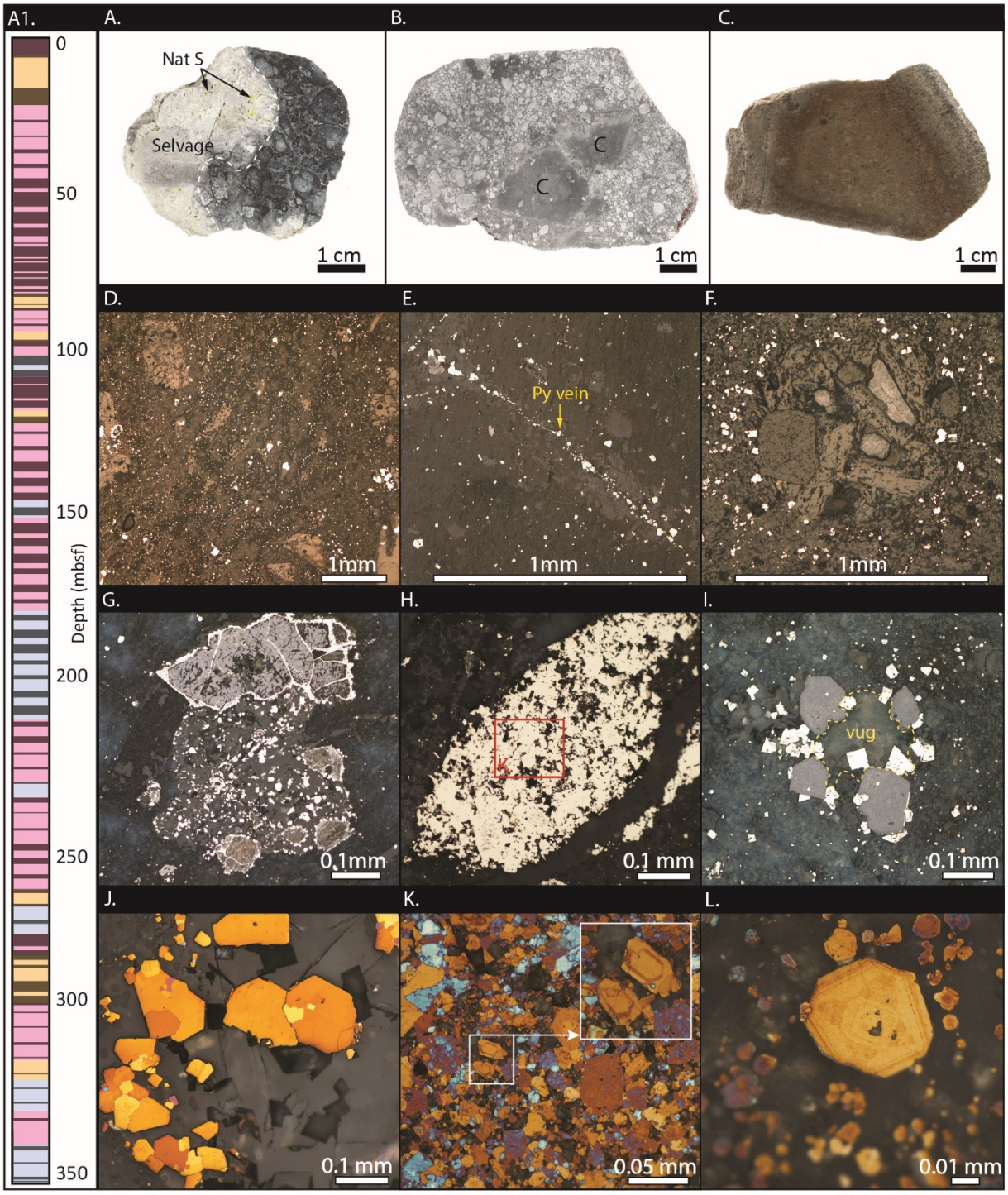

1023

1024

1025

1026

1027

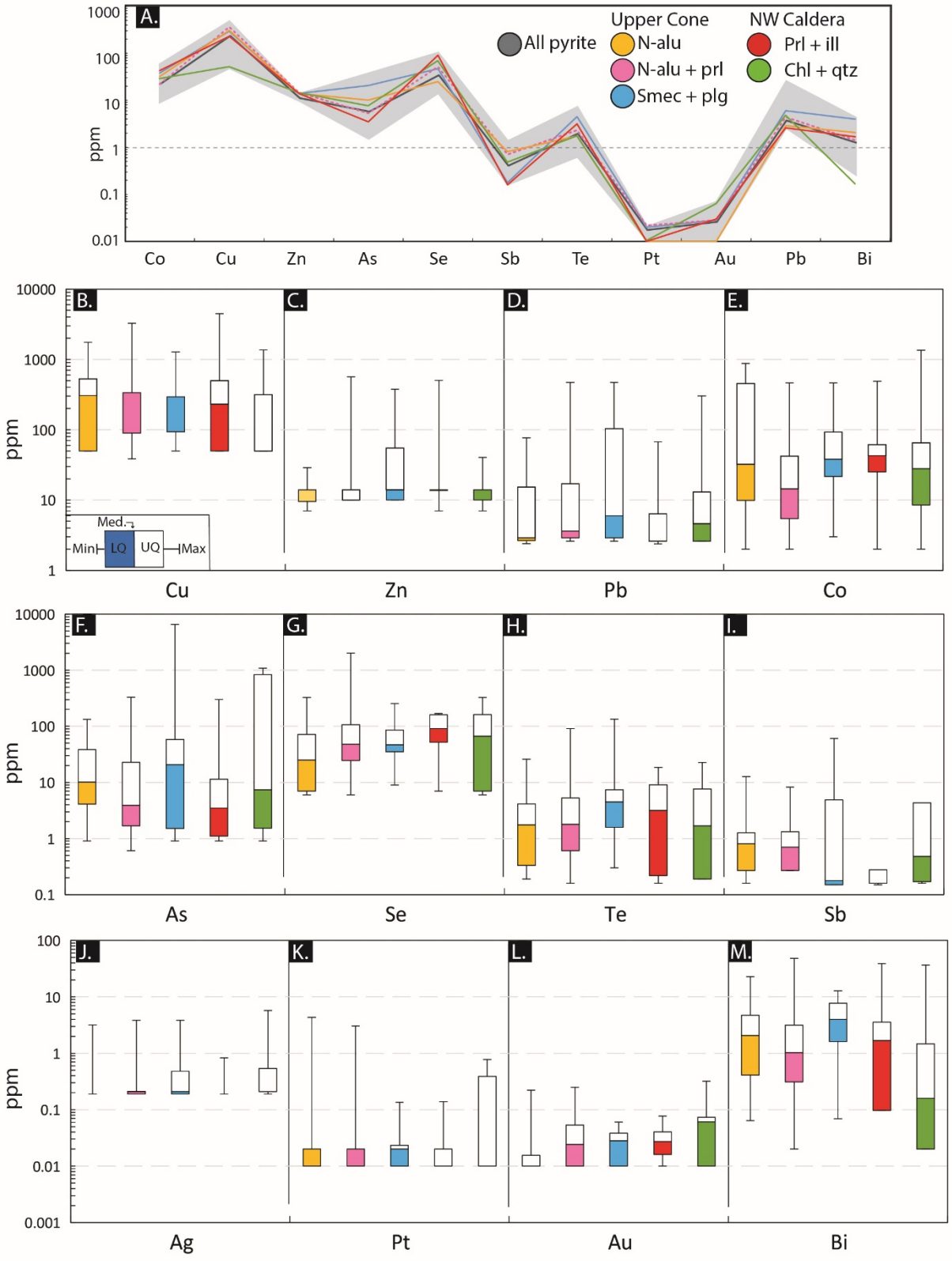
A.
All pyrite
Upper Cone
N-alu
N-alu + prl
Smec + plg
NW Caldera
Prl + ill
Chl + qtz
ppm
Co
Cu
Zn
As
Se
Sb
Te
Pt
Au
Pb
Bi
B.
C.
D.
E.
Med.
Min
LQ
UQ
Max
Cu
Zn
Pb
Co
F.
G.
H.
I.
As
Se
Te
Sb
J.
K.
L.
M.
Ag
Pt
Au
Bi

1028

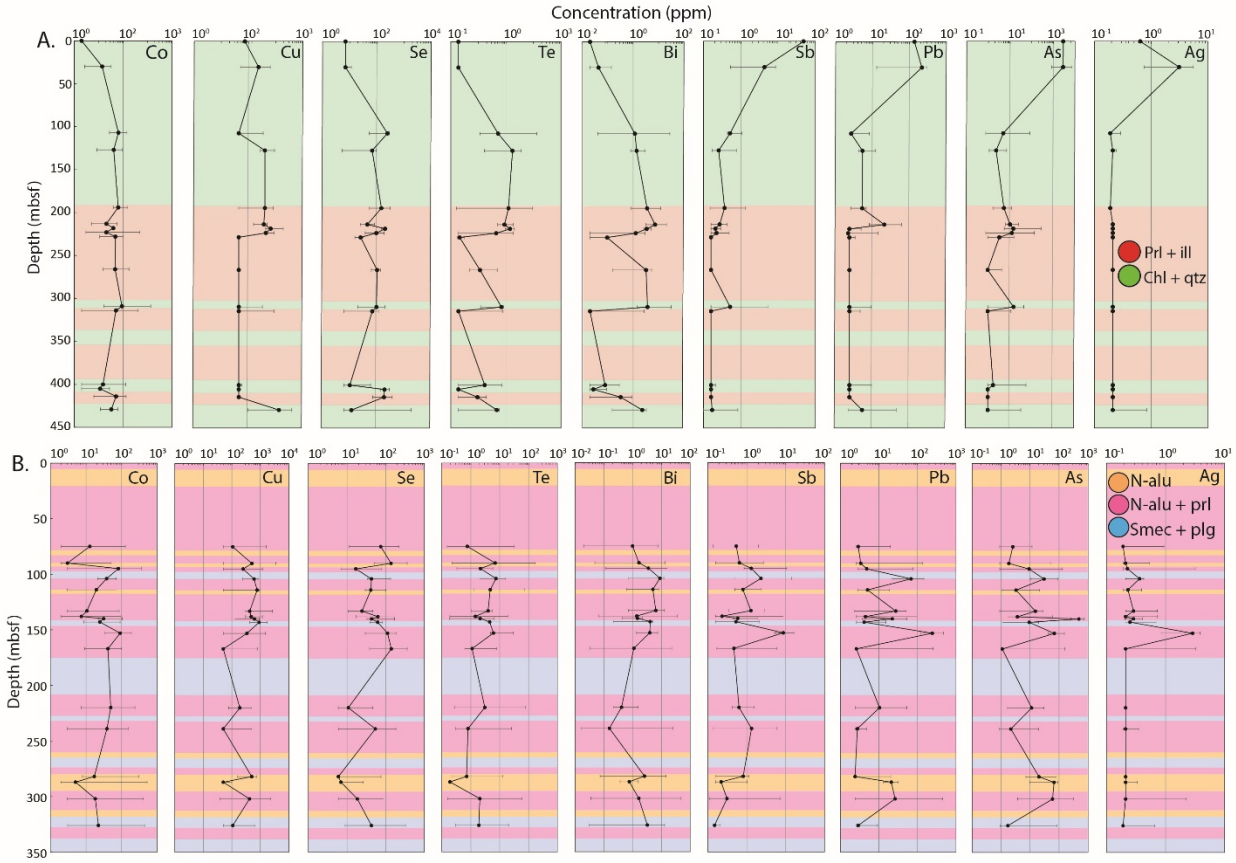
Concentration (ppm)
A.
Co
Cu
Se
Te
Bi
Sb
Pb
As
Ag
Depth (mbsf)
Prl + ill
Chl + qtz
B.
Co
Cu
Se
Te
Bi
Sb
Pb
As
Ag
Depth (mbsf)
N-alu
N-alu + prl
Smec + plg

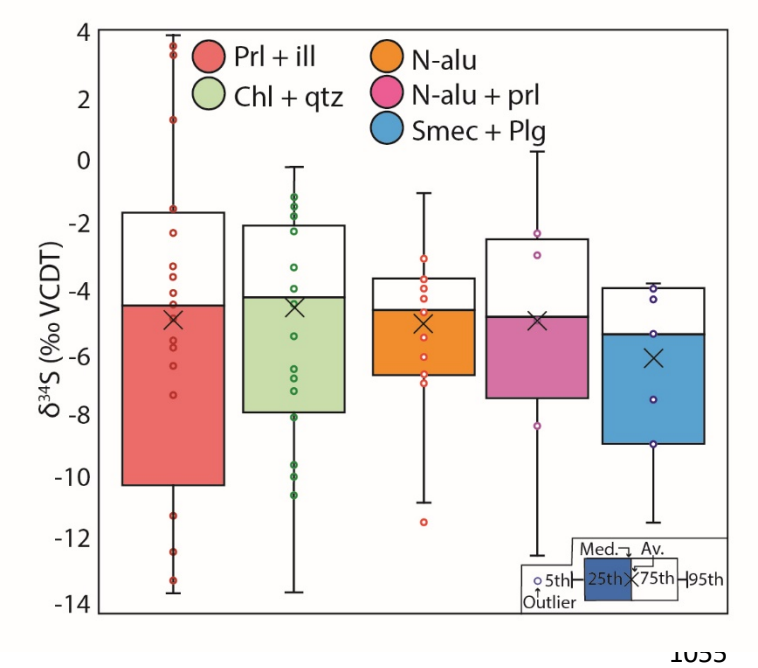
Prl + ill
Chl + qtz
N-alu
N-alu + prl
Smec + Plg
δ34S (‰ VCDT)
4
2
0
-2
-4
-6
-8
-10
-12
-14
Med.
Av.
5th
25th
75th
95th
Outlier

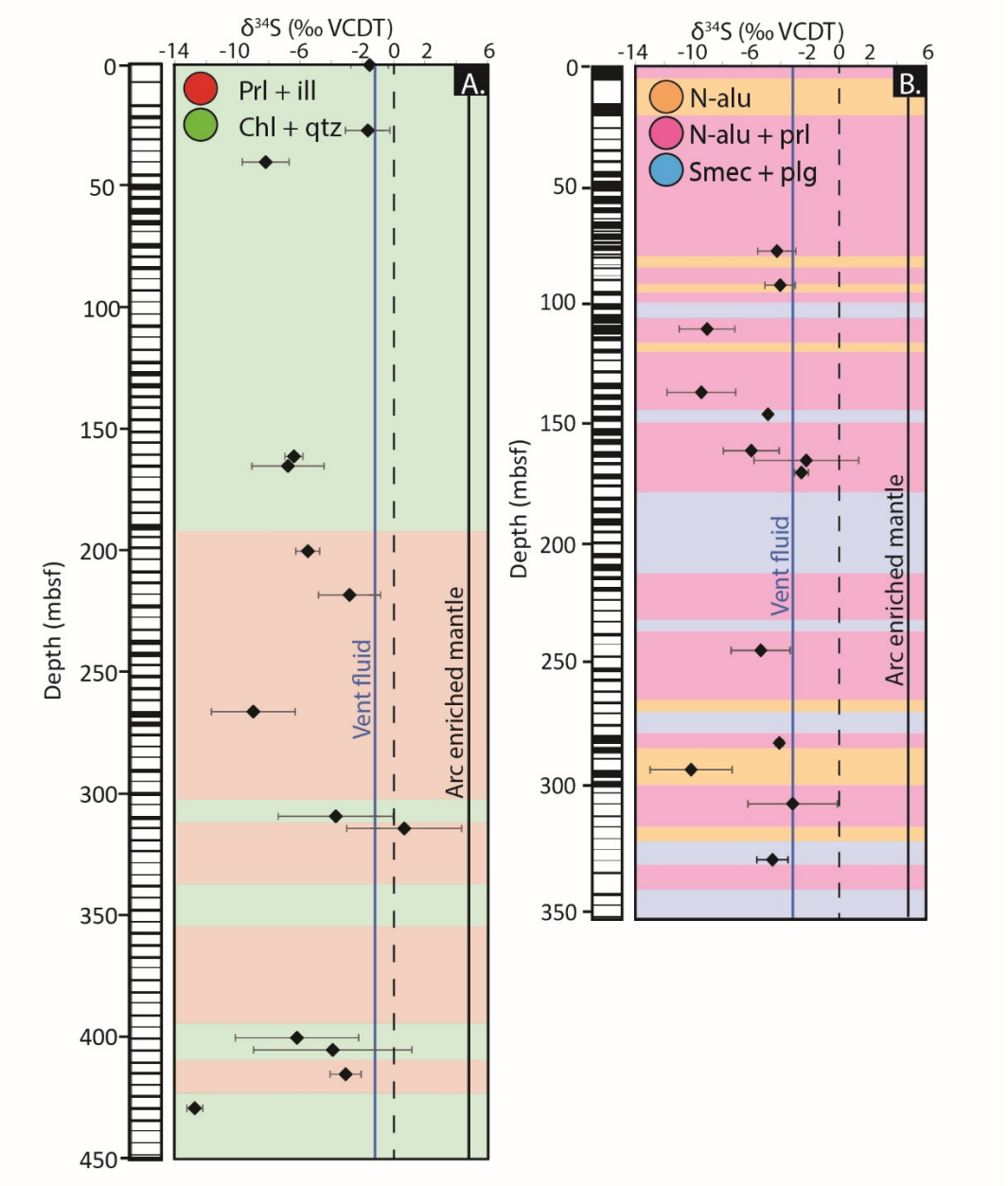
δ34S (‰ VCDT)
-14
-10
-6
-2
0
2
6
A.
Prl + ill
Chl + qtz
Vent fluid
Arc enriched mantle
Depth (mbsf)
0
50
100
150
200
250
300
350
400
450
B.
N-alu
N-alu + prl
Smec + plg

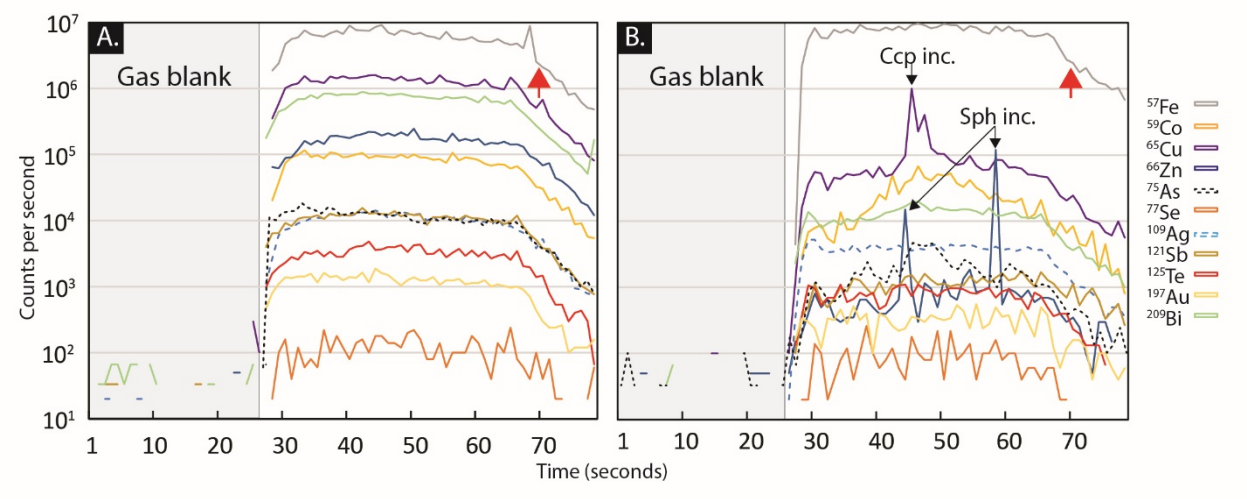
A.
Gas blank
B.
Gas blank
Ccp inc.
Sph inc.
Counts per second
Time (seconds)
57Fe
59Co
65Cu
66Zn
75As
77Se
109Ag
121Sb
125Te
197Au
209Bi

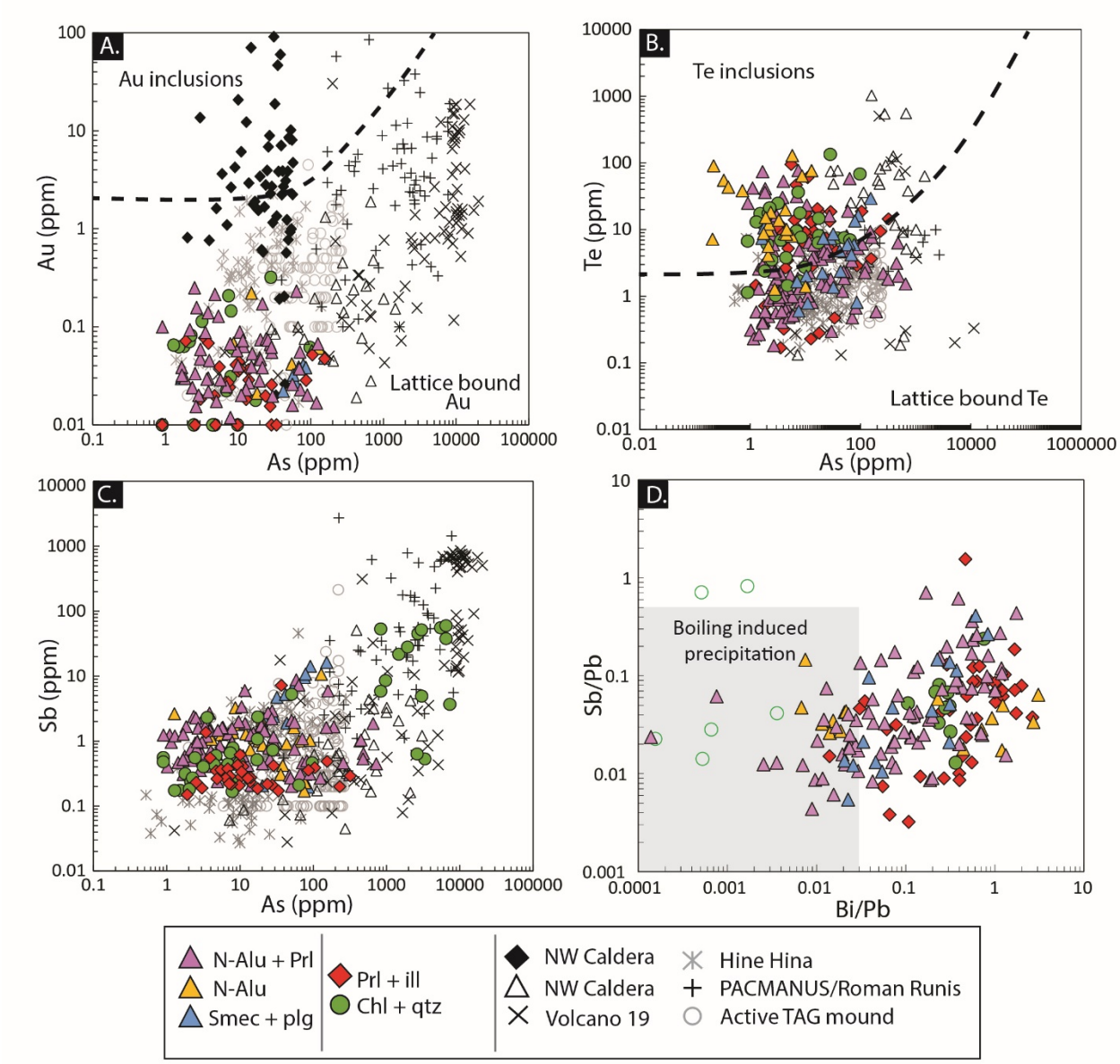

1124

1125

1126

1127

1128

1129

1130

1131

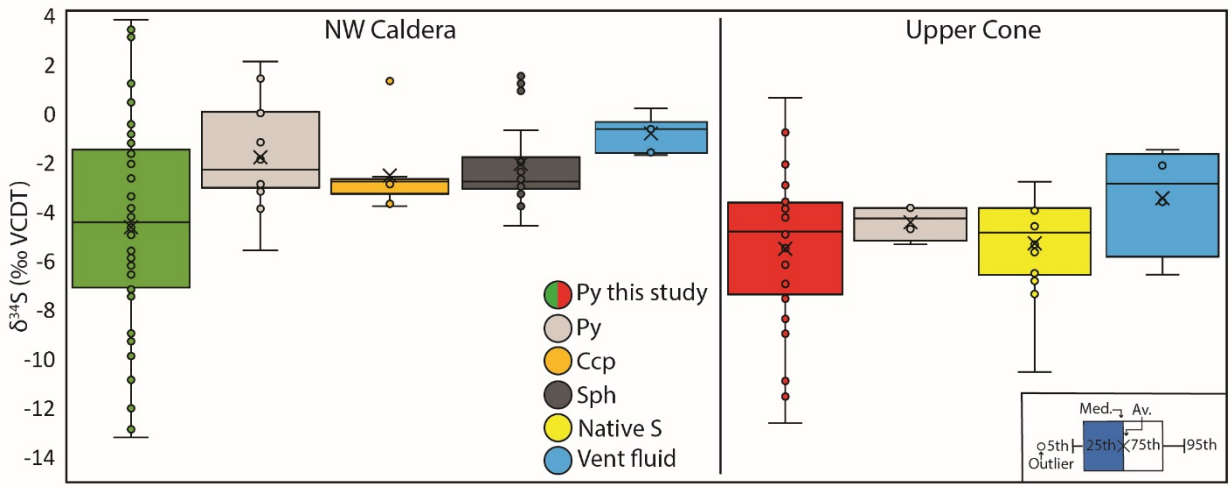
NW Caldera
Upper Cone
δ³⁴S (‰ VCDT)
4
2
0
-2
-4
-6
-8
-10
-12
-14
Py this study
Py
Ccp
Sph
Native S
Vent fluid
Med.
Av.
5th
25th
75th
95th
Outlier

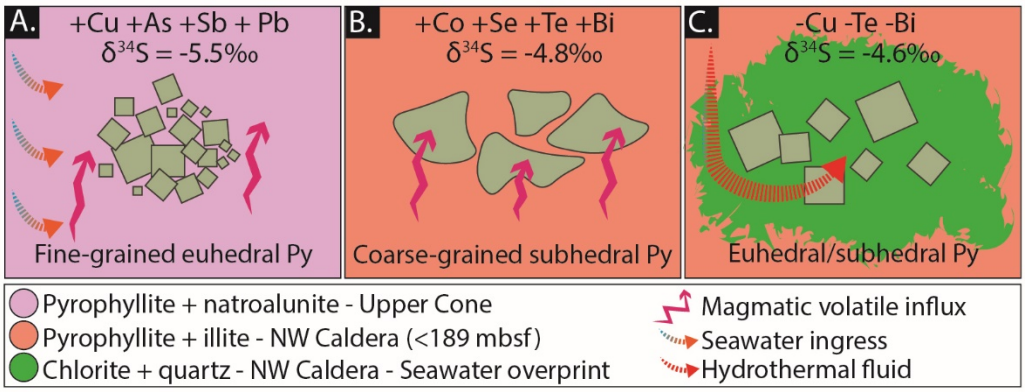
A.
+Cu +As +Sb + Pb
δ34S = -5.5‰
Fine-grained euhedral Py
B.
+Co +Se +Te +Bi
δ34S = -4.8‰
Coarse-grained subhedral Py
C.
-Cu -Te -Bi
δ34S = -4.6‰
Euhedral/subhedral Py
Pyrophyllite + natroalunite - Upper Cone
Pyrophyllite + illite - NW Caldera (<189 mbsf)
Chlorite + quartz - NW Caldera - Seawater overprint
Magmatic volatile influx
Seawater ingress
Hydrothermal fluid

1183

		Co	Ni	Cu	Zn	As	Se	Pd	Ag	Cd	Sb	Te	Re	Pt	Au	Pb	Bi
		ppm	wt%	wt%	ppm	ppm	ppm	ppm	ppm	ppm	ppm	ppm	ppm	ppm	ppm	ppm	ppm
NW Caldera																	
Chl + qtz	Av.	81.7	0.02	0.02	13.0	886.4	104.8	0.06	0.58	0.24	7.54	9.02	0.02	0.02	0.07	42.9	2.26
n=53	Med.	27.8	0.01	0.01	14.0	7.37	66.8	0.06	0.21	0.25	0.47	1.69	0.02	0.01	0.06	4.61	0.16
	Max	1351.7	0.05	0.10	40.3	7323.5	328.9	0.07	5.56	0.25	59.8	134.2	0.16	0.40	0.32	303.2	36.8
	σ	233.5	0.02	0.02	5.35	1853.0	107.9	0.00	1.03	0.01	16.5	20.9	0.02	0.06	0.08	79.1	6.61
Prl + ill	Av.	66.3	0.02	0.04	24.4	18.1	152.2	0.06	0.22	0.31	0.34	7.49	0.03	0.02	0.03	7.54	2.93
n=76	Med.	42.9	0.01	0.02	14.0	3.49	91.0	0.06	0.21	0.25	0.16	3.17	0.02	0.01	0.03	2.60	1.68
	Max	487.3	0.09	0.45	503.6	319.5	2075.4	0.09	0.83	4.21	7.20	94.9	0.42	0.14	0.08	67.2	23.7
	σ	85.0	0.02	0.07	59.0	49.1	270.1	0.01	0.07	0.46	0.82	14.03	0.05	0.02	0.02	11.9	4.29
Upper Cone																	
Smec + plg	Av.	82.1	0.01	0.04	44.9	33.5	75.7	0.06	0.76	0.24	3.06	6.20	0.02	0.03	0.03	76.9	4.86
n=28	Med.	38.1	0.01	0.03	14.0	20.6	47.0	0.06	0.21	0.22	0.18	4.51	0.02	0.02	0.03	6.01	3.99
	Max	463.7	0.01	0.15	376.3	152.8	342.2	0.15	3.84	0.46	16.3	29.3	0.05	0.14	0.06	471.0	12.8
	σ	101.5	0.00	0.03	76.6	38.1	71.7	0.02	1.12	0.04	4.70	6.72	0.01	0.04	0.02	126.0	4.01
N-alu + prl	Av.	45.4	0.02	0.04	31.0	38.8	74.7	0.06	0.39	0.26	1.42	8.25	0.07	0.05	0.04	32.5	3.23
n=151	Med.	20.3	0.01	0.03	13.5	4.87	47.5	0.06	0.21	0.25	0.65	2.12	0.02	0.02	0.03	4.01	1.31
	Max	463.7	0.05	0.35	563.0	727.8	362.5	0.15	3.84	1.79	16.3	170.1	1.58	3.04	0.25	471.0	48.1
	σ	76.3	0.02	0.05	71.4	99.5	72.8	0.01	0.61	0.14	2.51	20.1	0.14	0.24	0.04	79.0	5.54
N-alu	Av.	86.4	0.01	0.04	12.7	25.7	51.2	0.06	0.35	0.24	1.13	2.57	0.02	0.14	0.03	10.4	3.79
n=37	Med.	32.0	0.01	0.03	14.0	10.1	24.9	0.06	0.21	0.25	0.81	1.75	0.02	0.02	0.01	2.90	2.06
	Max	522.6	0.05	0.18	28.9	129.0	363.3	0.06	3.18	0.25	10.7	13.0	0.13	4.36	0.22	76.5	22.7
	σ	121.2	0.02	0.04	4.97	31.4	69.9	0.01	0.51	0.01	1.76	2.99	0.02	0.71	0.05	14.1	5.03

1184